COMPDYN 2015
5th ECCOMAS Thematic Conference on
Computational Methods in Structural Dynamics and Earthquake Engineering
M. Papadrakakis, V. Papadopoulos, V. Plevris (eds.)
Crete Island, Greece, 25–27 May 2015

APPLICATION OF THE PUSHOVER-BASED PROCEDURE TO PREDICT THE LARGEST PEAK RESPONSE OF ASYMMETRIC BUILDINGS WITH BUCKLING-RESTRAINED BRACES

Kenji Fujii

Department of Architecture and Civil Engineering, Chiba Institute of Technology
2-17-1 Tsudanuma, Narashino, Chiba 275-0016, Japan
e-mail: kenji.fujii@it-chiba.ac.jp

Keywords: Pushover Analysis, Asymmetric Buildings, Bidirectional Excitation, Buckling-restrained Braces

Abstract. *Asymmetric buildings are known to be vulnerable to earthquakes. This is because excessive deformation may occur at the frame of the flexible and/or weak side owing to an unfavourable torsional effect. Such deformation may lead to premature failure of the brittle members and finally to the collapse of whole buildings. To reduce the unfavourable torsional effect, one promising method is to install dampers to the frame in which excessive deformation is expected. The buckling-restrained brace (BRB) is widely used as a hysteresis damper in new buildings and for the seismic upgrading of existing buildings. For the evaluation of the peak seismic response of buildings, a pushover-based simplified procedure, which is often referred to as the nonlinear static procedure (NSP), has been developed and adopted to seismic design codes. In the case of reinforced concrete asymmetric buildings with BRBs, the first mode shape may notably change in the nonlinear range. This change may be critical in the accurate prediction of the peak response employing the NSP. However, there have been few studies on the applicability of NSPs to asymmetric buildings with BRBs. In this paper, the applicability of the simplified procedure proposed by the author to four-storey reinforced-concrete asymmetric buildings with BRBs is numerically investigated. In the simplified procedure presented in the previous study, the largest peak response is predicted from (a) the response of two independent equivalent single-degree-of-freedom models representing the first and second modes, considering the change in the first mode shape in each nonlinear stage, and (b) the envelope obtained from the combination of four pushover analyses considering the effect of bidirectional excitation. The predicted largest peak response is compared with the nonlinear time-history analysis results considering various directions of incidence of seismic input. The results show that the largest peak response of asymmetric buildings with BRBs is satisfactorily predicted by the procedure presented in the previous study. The effect of the change in mode shape on the accuracy of the NSP is also investigated and shown to be important in the accurate prediction of the peak response.*

1 INTRODUCTION

Asymmetric buildings are known to be vulnerable to earthquakes. This is because excessive deformation may occur at the frame of the flexible and/or weak side edge owing to an unfavourable torsional effect. This may lead to premature failure of the brittle members and finally to collapse of whole buildings. In general, the excessive deformation at the flexible and/or weak side frame can be reduced by relocation of frames and/or members. However, such relocation may not be feasible for existing buildings because of difficulties arising from architectural and functional constraints.

In recent years, the seismic rehabilitation of existing buildings using energy dissipative devices has been widely studied, and the seismic behaviour of asymmetric buildings with viscous, viscoelastic and elasto-plastic devices has been investigated [1–7]; the seismic behaviour of asymmetric buildings with viscous dampers has been investigated by Goel [1–3] and Chopra [4], while Landi [5] discussed the seismic design scheme of viscous dampers for the rehabilitation of an asymmetric building. De la Llera [6] discussed torsional balance, which is defined as the property of an asymmetric structure that leads to similar deformation demand in structural members equidistant from the geometric centre of the building plan, for elastic asymmetric structures with a friction damper. Mazza [7] discussed a displacement-based seismic design scheme of hysteresis dampers for rehabilitation of in-plan irregular reinforced concrete (RC) buildings. The results of these studies suggest that installation of dampers to the frame in which excessive deformation is expected is a promising method of reducing the unfavourable torsional effect of asymmetric buildings. However, in most of the above studies [1–6], asymmetric buildings are assumed to have linear (elastic) behaviour. Although Mazza [7] investigated the nonlinear behaviour of asymmetric buildings with a hysteresis damper by conducting nonlinear static (pushover) analyses, the results of pushover analyses and nonlinear dynamic (time-history) analyses have not been compared. Therefore, more investigations on the nonlinear behaviour of asymmetric buildings with various dampers are needed.

The pushover-based simplified nonlinear analysis procedure, which is often referred to as the nonlinear static procedure (NSP), has been developed by several researchers since the 1980s (e.g., [8], [9]). Although the application of the earlier version of the NSP is limited to planar frame analysis of buildings with regular elevation, the extension of the NSP to asymmetric buildings has been widely investigated in recent years (e.g., [10–16]). It would be valuable if these extended versions of the NSP were applicable to asymmetric buildings with dampers; however, there are problems. One critical problem, from the author's point of view, is that the unfavourable torsional effect is estimated from the linear elastic behaviour in most studies [10–13]. In the case of RC buildings with dampers, the first mode shape may change notably in the nonlinear range. Therefore, the estimation of the torsional effect based on linear elastic behaviour would lead to notable error in case of asymmetric buildings with dampers. In contrast, Bosco et al. [14] proposed a procedure of estimating the horizontal displacement distribution of asymmetric buildings from the envelope of two pushover analyses, using "corrective eccentricities". Even though this idea is attractive, proposed equations for the calculation of corrective eccentricities are based on numerical analyses of asymmetric structures without dampers. Therefore, it may be difficult to apply the idea directly to such asymmetric buildings with dampers. The author has investigated the development of the advanced NSP for asymmetric buildings considering by-directional excitation [15]. The author then proposed a simplified procedure that predicts the largest peak response of an asymmetric building to horizontal bidirectional ground motion acting at an arbitrary angle of incidence [16]. In this procedure, the largest peak response is predicted from (a) the response of two independent

equivalent single-degree-of-freedom (SDOF) models representing the first and second modes, considering the change in the first mode shape in each nonlinear stage, and (b) the envelope obtained from the combination of four pushover analyses considering the effect of bi-directional excitation. Because the effect of the change in mode shape in the nonlinear stage is considered in this procedure, the procedure has promise for application to an asymmetric building with dampers.

In this paper, the applicability of the simplified procedure proposed by the author [16] to four-storey RC asymmetric buildings with a hysteresis damper (buckling-restrained brace (BRB) [17, 18]) is numerically investigated. The predicted largest peak response is compared with the nonlinear dynamic (time-history) analysis results considering various directions of the incidence of seismic input. Note that the asymmetric buildings are limited to torsionally stiff (TS) buildings in this study.

2 DESCRIPTION OF THE SIMPLIFIED PROCEDURE TO PREDICT THE LARGEST PEAK RESPONSE

The simplified procedure presented by the author [16] is outlined in Figure 1. The asymmetric building considered in this study is an N-storey building, with $3N$ degrees of freedoms ($3N$-DOFs). All frames of the asymmetric building are oriented either the X- or Y-direction, which are mutually orthogonal. Another set of orthogonal axes U and V in the X–Y plane is considered, with the U-axis being the principal axis of the first modal response [15, 16]. This simplified procedure is detailed below on the basis of reference [16].

2.1 Step 1: Pushover analysis of the asymmetric building model (first mode)

A pushover analysis of an asymmetric building is carried out considering the change in the first mode shape. In this study, the displacement-based mode-adaptive pushover analysis (DB-MAP analysis presented in [16]) is applied. The nonlinear properties of the equivalent SDOF model and the relationship of the equivalent acceleration A_{1U}^{*} and equivalent displacement D_{1U}^{*}, referred to as the capacity curve, are then determined from the pushover analysis results.

The displacement vector at each loading stage $_{n}\mathbf{d}$ is assumed to be proportional to the first mode vector at each loading stage $_{n}\Gamma_{1U}\,{}_{n}\boldsymbol{\varphi}_{\mathbf{1}}$. The equivalent displacement and acceleration at each loading step n, $_{n}D_{1U}^{*}$ and $_{n}A_{1U}^{*}$, are then determined as

$$ {}_{n}D_{1U}^{*} = \frac{{}_{n}\Gamma_{1U}\,{}_{n}\boldsymbol{\varphi}_{\mathbf{1}}^{\mathrm{T}}\mathbf{M}_{\mathbf{n}}\mathbf{d}}{{}_{n}M_{1U}^{*}} = \frac{\sum_{j}\left(m_{j\,n}x_{j}^{2} + m_{j\,n}y_{j}^{2} + I_{j\,n}\theta_{j}^{2}\right)}{\sqrt{\left(\sum_{j}m_{j\,n}x_{j}\right)^{2} + \left(\sum_{j}m_{j\,n}y_{j}\right)^{2}}}, \tag{1} $$

$$ {}_{n}A_{1U}^{*} = \frac{{}_{n}\Gamma_{1U}\,{}_{n}\boldsymbol{\varphi}_{\mathbf{1}}^{\mathrm{T}}\,{}_{n}\mathbf{f}_{\mathbf{R}}}{{}_{n}M_{1U}^{*}} = \frac{\sum_{j}\left({}_{n}f_{RXjn}x_{j} + {}_{n}f_{RYjn}y_{j} + {}_{n}f_{MZj\,n}\theta_{j}\right)}{\sqrt{\left(\sum_{j}m_{j\,n}x_{j}\right)^{2} + \left(\sum_{j}m_{j\,n}y_{j}\right)^{2}}}, \tag{2} $$

where

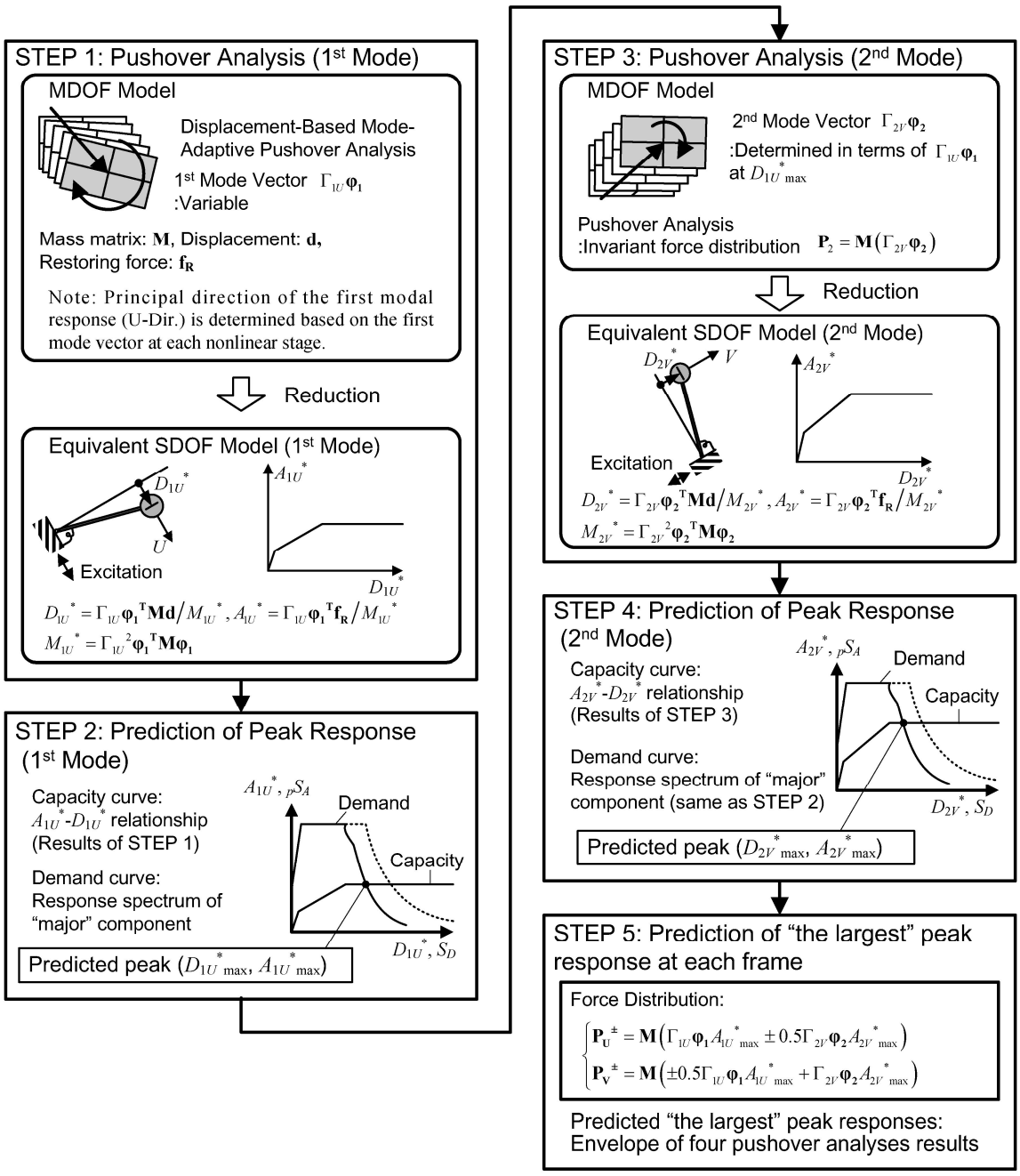

Figure 1: Outline of the simplified procedure

$$ {}_nM_{1U}^* = {}_n\Gamma_{1U}^2\,{}_n\boldsymbol{\varphi}_1^T\mathbf{M}_n\boldsymbol{\varphi}_1 = \frac{\left(\sum_j m_{j\,n}x_j\right)^2 + \left(\sum_j m_{j\,n}y_j\right)^2}{\sum_j\left(m_{j\,n}x_j^2 + m_{j\,n}y_j^2 + I_{j\,n}\theta_j^2\right)}, \tag{3} $$

$$ {}_n\Gamma_{1U} = \frac{{}_n\boldsymbol{\varphi}_1^T\mathbf{M}_n\boldsymbol{\alpha}_U}{{}_n\boldsymbol{\varphi}_1^T\mathbf{M}_n\boldsymbol{\varphi}_1} = \frac{\sqrt{\left(\sum_j m_{j\,n}x_j\right)^2 + \left(\sum_j m_{j\,n}y_j\right)^2}}{\sum_j\left(m_{j\,n}x_j^2 + m_{j\,n}y_j^2 + I_{j\,n}\theta_j^2\right)}, \tag{4} $$

$$\mathbf{M}=\begin{bmatrix}\mathbf{M_0} & \mathbf{0} & \mathbf{0}\\ \mathbf{0} & \mathbf{M_0} & \mathbf{0}\\ \mathbf{0} & \mathbf{0} & \mathbf{I_0}\end{bmatrix},\mathbf{M_0}=\begin{bmatrix}m_1 & & 0\\ & \ddots & \\ 0 & & m_N\end{bmatrix},\mathbf{I_0}=\begin{bmatrix}I_1 & & 0\\ & \ddots & \\ 0 & & I_N\end{bmatrix}, \tag{5}$$

$${}_{\mathbf{n}}\mathbf{d}=\left\{{}_nx_1 \quad \cdots \quad {}_nx_N \quad {}_ny_1 \quad \cdots \quad {}_ny_N \quad {}_n\theta_1 \quad \cdots \quad {}_n\theta_N\right\}^{\mathbf{T}}, \tag{6}$$

$${}_{\mathbf{n}}\mathbf{f_R}=\left\{{}_nf_{RX1} \quad \cdots \quad {}_nf_{RXN} \quad {}_nf_{RY1} \quad \cdots \quad {}_nf_{RYN} \quad {}_nf_{MZ1} \quad \cdots \quad {}_nf_{MZN}\right\}^{\mathbf{T}}, \tag{7}$$

$${}_{\mathbf{n}}\boldsymbol{\varphi}_{\mathbf{1}}=\left\{{}_n\phi_{X11} \quad \cdots \quad {}_n\phi_{XN1} \quad {}_n\phi_{Y11} \quad \cdots \quad {}_n\phi_{YN1} \quad {}_n\phi_{\Theta 11} \quad \cdots \quad {}_n\phi_{\Theta N1}\right\}^{\mathbf{T}}, \tag{8}$$

$${}_{\mathbf{n}}\boldsymbol{\alpha}_{\mathbf{U}}=\left\{\cos{}_n\psi_1 \quad \cdots \quad \cos{}_n\psi_1 \quad -\sin{}_n\psi_1 \quad \cdots \quad -\sin{}_n\psi_1 \quad 0 \quad \cdots \quad 0\right\}^{\mathbf{T}}, \tag{9}$$

$$\cos{}_n\psi_1=\frac{\sum_j m_j{}_n\phi_{Xj1}}{\sqrt{\left(\sum_j m_j{}_n\phi_{Xj1}\right)^2+\left(\sum_j m_j{}_n\phi_{Yj1}\right)^2}}=\frac{\sum_j m_j{}_nx_j}{\sqrt{\left(\sum_j m_j{}_nx_j\right)^2+\left(\sum_j m_j{}_ny_j\right)^2}}, \tag{10}$$

$$\sin{}_n\psi_1=\frac{-\sum_j m_j{}_n\phi_{Yj1}}{\sqrt{\left(\sum_j m_j{}_n\phi_{Xj1}\right)^2+\left(\sum_j m_j{}_n\phi_{Yj1}\right)^2}}=\frac{-\sum_j m_j{}_ny_j}{\sqrt{\left(\sum_j m_j{}_nx_j\right)^2+\left(\sum_j m_j{}_ny_j\right)^2}}. \tag{11}$$

In Eqs. (1)–(11), m_j and I_j are the mass and mass moment of inertia of the jth floor, respectively, ${}_nM_{1U}^*$ is the equivalent first modal mass with respect to the U-axis in each nonlinear stage, and ${}_n\psi_1$ is the angle of incidence of the U-axis in each nonlinear stage. Note that the reference axis considering the first modal response (U-axis) depends on the displacement; it changes in each nonlinear stage as the first mode vector changes.

2.2 Step 2: Prediction of the peak response of the equivalent SDOF model (first mode)

The largest peak equivalent displacement $D_{1U}{}^*{}_{\max}$ and equivalent acceleration $A_{1U}{}^*$ are obtained using the equivalent linearization technique [19]. The equivalent period and the equivalent damping ratio of the equivalent SDOF model in each loading stage n, ${}_nT_{1eq}$ and ${}_nh_{1eq}$ respectively, are determined as

$${}_nT_{1eq}=2\pi\sqrt{\frac{{}_nD_{1U}^*}{{}_nA_{1U}^*}}=2\pi\sqrt{\frac{\sum_j\left(m_j{}_nx_j^2+m_j{}_ny_j^2+I_j{}_n\theta_j^2\right)}{\sum_j\left({}_nf_{RXj}{}_nx_j+{}_nf_{RYj}{}_ny_j+{}_nf_{MZj}{}_n\theta_j\right)}}, \tag{12}$$

$${}_nh_{1eq}=\frac{\sum_k{}_nh_{eqFk}{}_nW_{eFk}+\sum_l{}_nh_{eqDl}{}_nW_{eDl}}{\sum_k{}_nW_{eFk}+\sum_l{}_nW_{eDl}}, \tag{13}$$

where

$$ {}_{n}h_{eqFk} = \begin{cases} h_0 \sqrt{\dfrac{{}_{n}K_{EQFk}}{K_{EFk}}} & : {}_{n}\mu_{Fk} \le 1 \\ 0.25\left(1 - \dfrac{1}{\sqrt{{}_{n}\mu_{Fk}}}\right) + h_0 \sqrt{\dfrac{{}_{n}K_{EQFk}}{K_{EFk}}} & : {}_{n}\mu_{Fk} \ge 1 \end{cases}, \tag{14} $$

$$ {}_{n}h_{eqDl} = \begin{cases} 0 & : {}_{n}\mu_{Dl} \le 1 \\ 0.6 \times \dfrac{2}{\pi}\left(1 - \dfrac{1}{{}_{n}\mu_{Dl}}\right) & : {}_{n}\mu_{Dl} \ge 1 \end{cases}. \tag{15} $$

In Eqs. (12)–(15), ${}_{n}h_{eqFk}$, ${}_{n}W_{eFk}$ and ${}_{n}\mu_{Fk}$ are the equivalent damping ratio, potential energy, and ductility ratio of the kth nonlinear spring of the RC member, respectively; ${}_{n}h_{eqDl}$, ${}_{n}W_{eDl}$ and ${}_{n}\mu_{Dl}$ are the equivalent damping ratio, potential energy, and ductility ratio of the lth nonlinear spring of the hysteresis damper, respectively; and h_0 is the initial damping ratio, which is assumed to be 0.03 in this study.

The spectral reduction factor relating to the equivalent damping ratio, $F({}_{n}h_{1eq})$, is determined as

$$ F\left({}_{n}h_{1eq}\right) = \frac{{}_{p}S_A\left({}_{n}T_{1eq}, {}_{n}h_{1eq}\right)}{{}_{p}S_A\left({}_{n}T_{1eq}, 0.05\right)} = \frac{S_D\left({}_{n}T_{1eq}, {}_{n}h_{1eq}\right)}{S_D\left({}_{n}T_{1eq}, 0.05\right)} = \frac{1.5}{1 + 10\,{}_{n}h_{1eq}}, \tag{16} $$

where ${}_{p}S_A$ (${}_{n}T_{1eq}$, ${}_{n}h_{1eq}$) and S_D (${}_{n}T_{1eq}$, ${}_{n}h_{1eq}$) are the psuedo spectral acceleration and the spectral displacement of ground motion, respectively. In this study, the curve of the ${}_{p}S_A$ (${}_{n}T_{1eq}$, ${}_{n}h_{1eq}$)–S_D (${}_{n}T_{1eq}$, ${}_{n}h_{1eq}$) relationship is referred to as the demand curve.

For the prediction of the "largest" peak response, it is assumed that the spectra of two horizontal ground motion components are identical: the spectrum of the horizontal minor component is assumed to be the same as that of the major component. Therefore, the same response spectra are used to predict the peak responses of the first and second modes.

The predicted peak response ($D_{1U}{}^{*}_{\max}$, $A_{1U}{}^{*}_{\max}$) is obtained as the intersection point of the capacity curve and demand curve.

2.3 Step 3: Pushover analysis of the asymmetric building model (second mode)

From the results of Steps 1 and 2, the first mode vector corresponding to $D_{1U}{}^{*}_{\max}$, $\Gamma_{1Uie}\boldsymbol{\varphi}_{\mathbf{1ie}}$, is obtained. The second mode vector, $\Gamma_{2Vie}\boldsymbol{\varphi}_{\mathbf{2ie}}$, is then determined in terms of $\Gamma_{1Uie}\boldsymbol{\varphi}_{\mathbf{1ie}}$ and the second mode vector in the elastic range, $\boldsymbol{\varphi}_{\mathbf{2e}}$, considering the orthogonal condition of the mode vector, as

$$ \Gamma_{2Vie} = \frac{\boldsymbol{\varphi}_{\mathbf{2ie}}{}^{\mathrm{T}}\mathbf{M}\boldsymbol{\alpha}_{\mathbf{Vie}}}{\boldsymbol{\varphi}_{\mathbf{2ie}}{}^{\mathrm{T}}\mathbf{M}\boldsymbol{\varphi}_{\mathbf{2ie}}}, \boldsymbol{\varphi}_{\mathbf{2ie}} = \boldsymbol{\varphi}_{\mathbf{2e}} - \frac{\boldsymbol{\varphi}_{\mathbf{2e}}{}^{\mathrm{T}}\mathbf{M}\boldsymbol{\varphi}_{\mathbf{1ie}}}{\boldsymbol{\varphi}_{\mathbf{1ie}}{}^{\mathrm{T}}\mathbf{M}\boldsymbol{\varphi}_{\mathbf{1ie}}}\boldsymbol{\varphi}_{\mathbf{1ie}}, \tag{17} $$

where

$$ \boldsymbol{\alpha}_{\mathbf{Vie}} = \left\{\sin\psi_{1ie} \;\cdots\; \sin\psi_{1ie} \;\; \cos\psi_{1ie} \;\cdots\; \cos\psi_{1ie} \;\; 0 \;\cdots\; 0\right\}^{\mathrm{T}}, \tag{18} $$

$$\cos\psi_{1ie}=\frac{\sum_j m_j\phi_{Xj1ie}}{\sqrt{\left(\sum_j m_j\phi_{Xj1ie}\right)^2+\left(\sum_j m_j\phi_{Yj1ie}\right)^2}},\ \sin\psi_{1ie}=\frac{-\sum_j m_j\phi_{Yj1ie}}{\sqrt{\left(\sum_j m_j\phi_{Xj1ie}\right)^2+\left(\sum_j m_j\phi_{Yj1ie}\right)^2}}. \quad (19)$$

Next, another pushover analysis of the asymmetric building is carried out to obtain the force–displacement relationship representing the second mode response by applying the invariant force distribution $\mathbf{P_2}$ determined as

$$\mathbf{P_2}=\mathbf{M}\left(\Gamma_{2Vie}\boldsymbol{\varphi}_{\mathbf{2ie}}\right). \quad (20)$$

The equivalent displacement ${}_nD_{2V}{}^*$ and acceleration ${}_nA_{2V}{}^*$ of the equivalent SDOF model representing the second mode response at each loading step n are determined as

$${}_nD_{2V}{}^*=\frac{\Gamma_{2Vie}\boldsymbol{\varphi}_{\mathbf{2ie}}{}^{\mathbf{T}}\mathbf{M}_{\mathbf{n}}\mathbf{d}}{M_{2Vie}{}^*},\ {}_nA_{2V}{}^*=\frac{\Gamma_{2Vie}\boldsymbol{\varphi}_{\mathbf{2ie}}{}^{\mathbf{T}}{}_{\mathbf{n}}\mathbf{f}_{\mathbf{R}}}{M_{2Vie}{}^*}, \quad (21)$$

$$M_{2Vie}{}^*=\Gamma_{2Vie}{}^2\boldsymbol{\varphi}_{\mathbf{2ie}}{}^{\mathbf{T}}\mathbf{M}\boldsymbol{\varphi}_{\mathbf{2ie}}. \quad (22)$$

In Eq. (22), $M_{2Vie}{}^*$ is the equivalent second modal mass with respect to the V-axis determined in terms of $\Gamma_{2Vie}\boldsymbol{\varphi}_{\mathbf{2ie}}$.

2.4 Step 4: Prediction of the peak response of the equivalent SDOF model (second mode)

The largest peak equivalent displacement $D_{2V}{}^*{}_{\max}$ and the equivalent acceleration $A_{2V}{}^*{}_{\max}$ for the second mode response are obtained using the equivalent linearization technique as discussed in Step 2. Note that for the calculation of the equivalent damping ratio of the second mode, the initial damping ratio used in Eq. (14), h_0, is assumed to be the same as that assumed in Step 2 for the first mode. The same spectrum used in Step 2 is used again for the prediction of the second mode response.

2.5 Step 5: Prediction of the largest peak response at each frame

The four force distributions are determined as the sum of the contributions of the first and second mode responses. The largest peak response is predicted as the envelope of the four pushover analyses results. Details of the largest peak response prediction at each frame are described as follows.

1) Determine the four combined forces $\mathbf{P_U}^+$, $\mathbf{P_U}^-$, $\mathbf{P_V}^+$, $\mathbf{P_V}^-$, according to

$$\begin{cases}\mathbf{P_U}^{\pm}=\mathbf{M}\left(\Gamma_{1Uie}\boldsymbol{\varphi}_{\mathbf{1ie}}A_{1U}{}^*{}_{\max}\pm 0.5\Gamma_{2Vie}\boldsymbol{\varphi}_{\mathbf{2ie}}A_{2V}{}^*{}_{\max}\right)\\ \mathbf{P_V}^{\pm}=\mathbf{M}\left(\pm 0.5\Gamma_{1Uie}\boldsymbol{\varphi}_{\mathbf{1ie}}A_{1U}{}^*{}_{\max}+\Gamma_{2Vie}\boldsymbol{\varphi}_{\mathbf{2ie}}A_{2V}{}^*{}_{\max}\right)\end{cases}. \quad (23)$$

2) Perform pushover analyses using $\mathbf{P_U}^+$, $\mathbf{P_U}^-$ until the equivalent displacement ${}_nD_U{}^*$ calculated using Eq. (24) reaches $D_{1U}{}^*{}_{\max}$, obtained from Step 2 (referred to as Pushover-1U and 2U, respectively); similarly, $\mathbf{P_V}^+$, $\mathbf{P_V}^-$ are used in the analysis until the equivalent displacement ${}_nD_V{}^*$ calculated from Eq. (24) reaches $D_{2V}{}^*{}_{\max}$, obtained from Step 4 (referred to as Pushover-1V and 2V, respectively). Equation (24) is

$$ {}_nD_U^* = \frac{\Gamma_{1Uie}\boldsymbol{\varphi}_{\mathbf{1ie}}{}^{\mathrm{T}}\mathbf{M}_{\mathbf{n}}\mathbf{d}}{M_{1Uie}^*}, \; {}_nD_V^* = \frac{\Gamma_{2Vie}\boldsymbol{\varphi}_{\mathbf{2ie}}{}^{\mathrm{T}}\mathbf{M}_{\mathbf{n}}\mathbf{d}}{M_{2Vie}^*}, \tag{24} $$

where

$$ M_{1Uie}^* = \Gamma_{1Uie}{}^2\boldsymbol{\varphi}_{\mathbf{1ie}}{}^{\mathrm{T}}\mathbf{M}\boldsymbol{\varphi}_{\mathbf{1ie}} . \tag{25} $$

In Eq. (24), M_{1Uie}^* is the equivalent first modal mass with respect to the U-axis determined in terms of $\Gamma_{1Uie}\boldsymbol{\varphi}_{\mathbf{1ie}}$.

3) Determine the largest peak response at each frame from the envelope of (a) Pushover-1U and 2U and (b) Pushover-1V and 2V.

3 BUILDING AND GROUND MOTION DATA

3.1 Building data

3.1.1. Building model without BRBs

The building investigated in this study is a four-storey asymmetric building model as shown in Figure 2. This building model, with bi-directional eccentricity, is the same as Model-B1 in the previous study [16]. In the present study, this building model (without BRBs) is referred to as Model-O.

The floor mass m_j and moment of inertia I_j (j = 1–4) are assumed as 525t and 4.37×10^4 tm^2, respectively. The columns are assumed to have fixed ends supported by the foundation. The compressive strength of concrete, σ_B, is assumed to be 24 N/mm^2. In addition, SD345 steel (yield strength σ_y = 345 N/mm^2) is used for the longitudinal reinforcement, and SD295 steel (σ_y = 295 N/mm^2) is used for the shear reinforcement and wall and slab reinforcement. Each frame structure was designed according to the weak-beam, strong-column concept; the longitudinal reinforcement of the concrete section is determined so that potential hinges are located at the beam ends and the bottoms of the columns and the structural walls in the first storey. Sufficient shear reinforcement is assumed to be provided to prevent premature shear failure. Table 1 gives the longitudinal reinforcement for each member. The crack moment M_c and yield moment M_y of each member are calculated according to the AIJ Design Guideline [20]. The base shear coefficients obtained from the planar pushover analysis in the X- and Y-directions, which are the values when the roof displacement reaches 1% of the total height H_N (= 14.8 m), were 0.522 and 0.455, respectively.

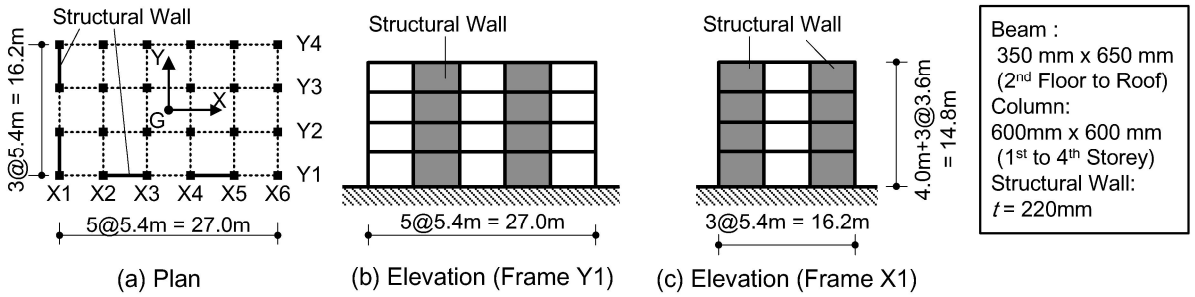

Figure 2: Model building without BRBs (Model-O)

Member	Location	Reinforcement
Boundary beam	2nd to roof floor	6-D25 (top and bottom)
Beam	4th and roof floor 2nd to 3rd floor	3-D25 (top and bottom) 4-D25 (top and bottom)
Column	2nd to 4th storey 1st storey	20-D29 (top and bottom) 20-D29 (top), 8-D29 (bottom)
Structural Wall	All storey	D10@200Double

Table 1: Longitudinal reinforcement of each member

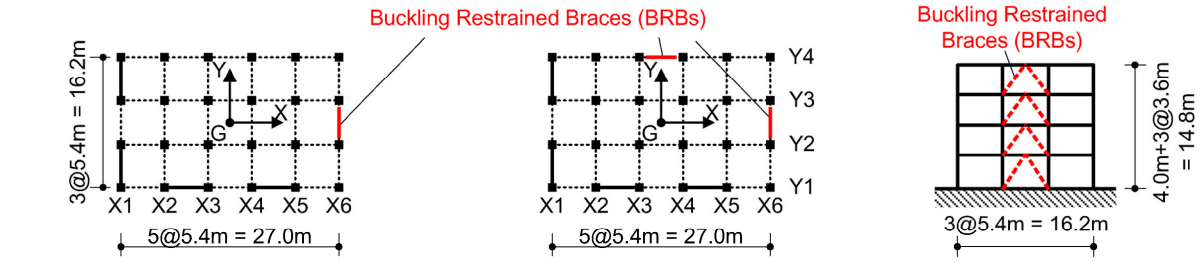

(a) Plan (Model-BRB1L, Model-BRB1H) (b) Plan (Model-BRB2L, Model-BRB2H) (c) Elevation (Frame X6)

Figure 3: Model building with BRBs (Model-BRB1L, BRB1H, BRB2L and BRB2H)

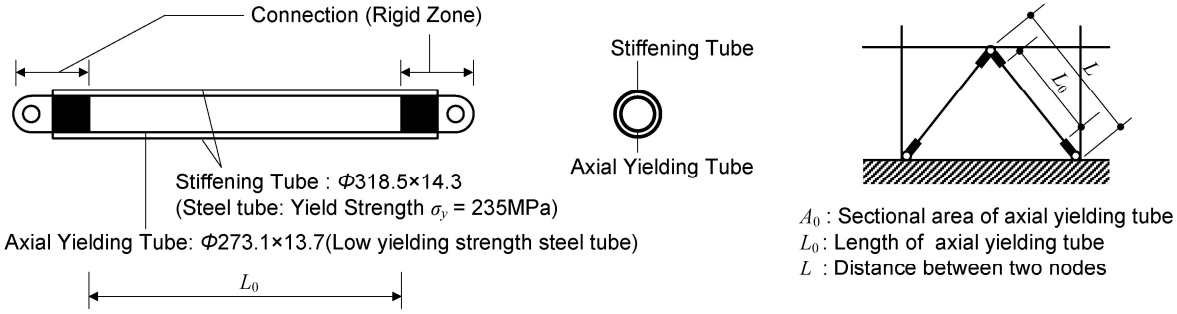

(a) Buckling Restrained Brace (BRB) (b) Frame with BRBs

Figure 4: Configuration of BRB

3.1.2. Building models with BRBs

In this study, Model-O was rehabilitated by installing BRBs, and the four rehabilitated building models shown in Figure 3 were investigated: two rehabilitated building models with BRBs in Frame X6, which is the flexible edge frame in the Y-direction (Model-BRB1L, BRB1H), and two with BRBs in Frames Y4 and X6, which are the flexible edge frames in both X- and Y-directions, respectively (Model-BRB2L, BRB2H). Figure 4 shows the configuration of BRBs installed in the rehabilitated model. As shown in Figure 4 (a), the tube-in-tube BRB [17, 18] was used in this study. In this brace, an axial yielding tube (a steel tube with low yielding strength) inside the brace yields and absorbs the hysteresis energy, while a stiffening tube outside the brace prevents the premature buckling of the axial yielding tube. The dimensions of the axial yielding tube were the same for all storeys. In this study, two grades of yield strength σ_y were assumed for the axial yielding tube: σ_y was assumed as 80 N/mm^2 for Model-BRB1L and BRB2L and 205 N/mm^2 for Model-BRB1H and BRB2H. Therefore, the yield axial force, N_y, of the BRBs used in Model-BRB1L and BRB2L is 893 kN while that of the BRBs used in Model-BRB1H and BRB2H is 2290 kN.

Figure 4(b) shows the frame with BRBs. Because the end connection of the BRB is considered a rigid zone, the axial stiffness of the BRB is increased by the ratio (L/L_0), where L

and L_0 are the distance between two nodes and the length of the axial yielding tube (shown in Figure 4), respectively. In the case of actual BRBs, there is "deformation loss" due to, for example, gaps of pin connections and deformations of joints. In this study, the axial stiffness of the BRB is determined from the sectional area of the axial yielding tube A_0 and L, for the simplicity of analysis.

3.1.3. Modelling of building structures

The building structures are modelled as a psuedo three-dimensional frame model in which the floor diaphragms are assumed to be rigid in their own planes with no out-of-plane stiffness, and the frames oriented in the X- and Y-directions are modelled independently. One-component model, with one nonlinear flexural spring at both ends and one nonlinear shear spring in the middle of the line element, is used for all concrete beams, columns and structural walls. At the end of each member, rigid zones are assumed, and the rigid zone length is determined as follows. For the beams (except the boundary beam) and columns, the rigid zone length is assumed as half the depth of the intersecting member minus one-fourth of the depth of the considered member itself, and the rigid zone length on the wall-side of the boundary beam is assumed as half the column-centre to column-centre length of the structural wall. For the structural walls, no rigid zone is considered at either end. To determine the flexibility of the nonlinear flexural springs, an anti-symmetric curvature distribution is assumed for the beams and columns, and a uniform curvature distribution is assumed for the structural walls. The BRBs are modelled as a line element with a pin at both ends, and a nonlinear axial spring in the middle of the line element.

Figure 5 shows the envelope curve for the force–deformation relationship of each nonlinear spring. The envelopes are assumed to be symmetric in both the positive and negative loading directions. In Figure 5(a), the secant stiffness degradation ratio of the flexural spring at the yield point, α_y, is assumed to be 0.25 for all beams and columns. For the structural walls at the bottom of the first storey, α_y is assumed to be 0.12. At all other ends of structural walls, α_y is assumed to be 0.19. In Figure 5(b), the secant stiffness degradation ratio of the shear spring at the "yield point" β_y is assumed to be 0.16. The axial behaviour of the concrete columns and structural walls is assumed to remain elastic, and the effects of the biaxial bending and axial-flexural interaction are ignored. Braces (BRBs) are modelled as a line element with a pin connection at both ends, and the envelope of the axial force (N)–axial deformation (e) relationship is shown in Figure 5(c). The torsional stiffness of the members is ignored. No second-order effect (e.g., the P-Δ effect) is considered.

Figure 6 shows the hysteresis model used for each nonlinear spring. The Muto hysteretic model [21] with one modification is used to model the flexural spring, as shown in Figure 6 (a). Specifically, the unloading stiffness after yielding decreases in proportion to $\mu^{-0.5}$ (where μ is the ductility ratio of the flexural spring) to represent the degradation of the unloading stiffness after yielding of the RC members, as in the model of Otani [22]. The origin-

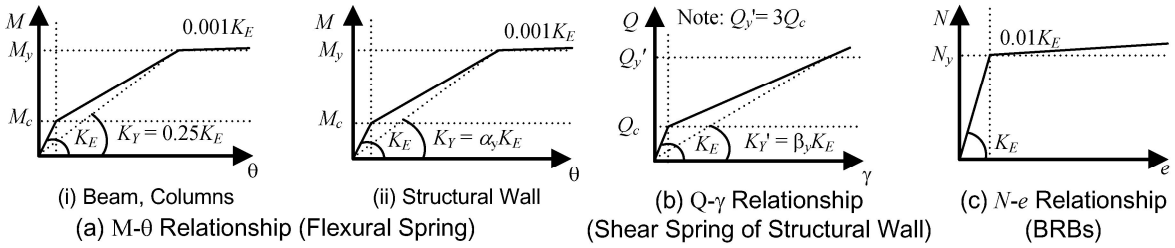

Figure 5: Envelope of the force–deformation relationship of nonlinear springs

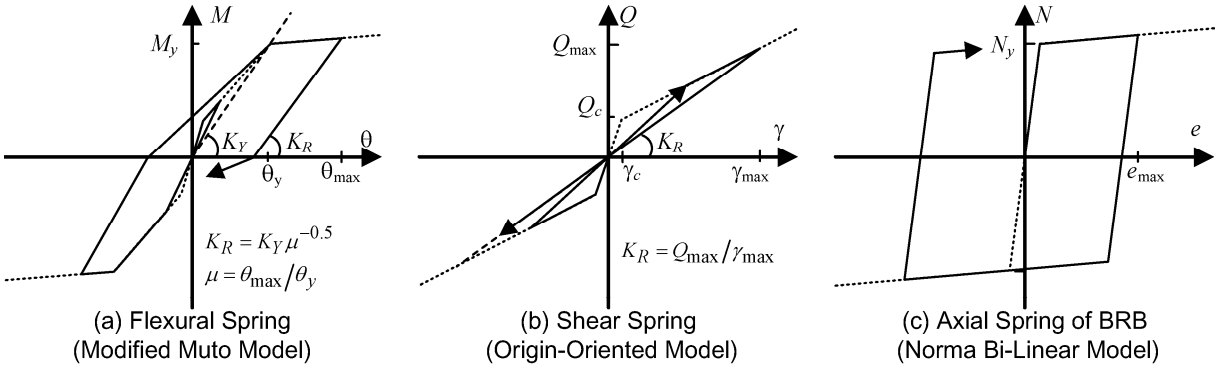

Figure 6: Hysteresis model for the nonlinear springs

oriented model (Figure 6 (b)) is used to model the shear spring of the structural wall. The shear spring of the beams and columns is assumed to be elastic. The normal bilinear hysteretic model (Figure 6 (c)) is used to model the axial spring of the BRBs.

In this study, the damping matrix at time t, $\mathbf{C}(t)$, is assumed to be proportional to the instant stiffness matrix without BRBs $\mathbf{K_{Tf}}(t)$ as expressed by

$$\mathbf{C}(t) = \left(2h_{1f}/\omega_{1ef}\right)\mathbf{K_{Tf}}(t), \tag{26}$$

where ω_{1ef} and h_{1f} are the elastic natural circular frequency and damping ratio of the first mode of the model without BRBs, respectively. In this study, h_{1f} is assumed to be 0.03.

3.1.4. Natural modes of the building models

Figure 7 shows the natural modes of the building models in the elastic range. Here, T_{ie} is the ith natural period in the elastic range, ψ_{ie} is the angle of incidence of the principal direction of the ith modal response in the elastic range with its tangent given by

$$\tan\psi_{ie} = -\sum_j m_j\phi_{Yjie} \Big/ \sum_j m_j\phi_{Xjie}, \tag{27}$$

and $R_{\rho ie}$ is the torsional index of the ith mode [23] in the elastic range, as defined by

$$R_{\rho ie} = \sqrt{\sum_j I_j\phi_{\Theta jie}{}^2 \Big/ \left(\sum_j m_j\phi_{Xjie}{}^2 + \sum_j m_j\phi_{Yjie}{}^2\right)}. \tag{28}$$

Note that, in the elastic range, the natural modes of Model-BRB1L and BRB1H are mutually the same, and those of Model-BRB2L and BRB2H are also mutually the same. This is because the elastic axial stiffness is the same for all BRBs used in this study. As shown in Figure 7, the principal direction of the first three modes is not along the X- and Y-axes in any of the building models, and the differences in natural modes among building models are very small; a significant difference can be found only in the natural period of the first mode. In all building models, the first mode is predominantly translational $\left(R_{\rho 1e} < 1\right)$, the second mode is almost purely translational $\left(R_{\rho 2e} \ll 1\right)$, while the third mode is predominantly torsional $\left(R_{\rho 3e} > 1\right)$, and the angle between the principal directions of the first two modes is close to 90° (within 90.2°–99.7°). Because the first and second modes are predominantly translational

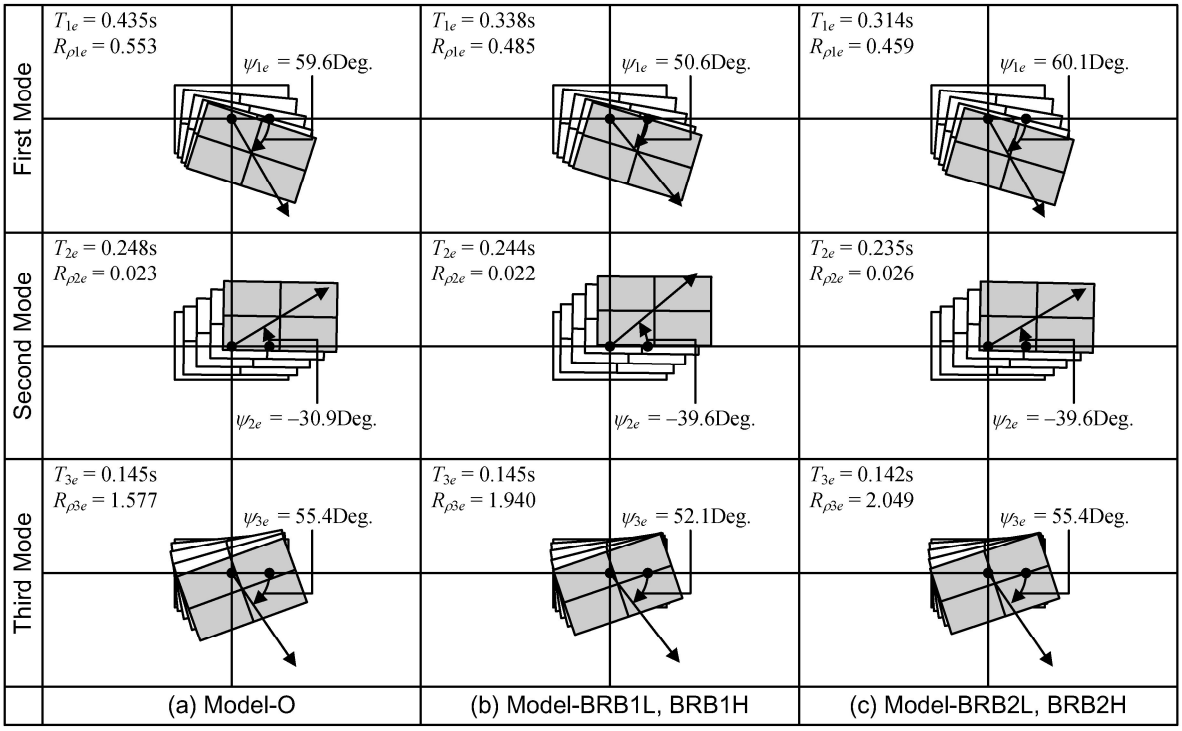

Figure 7: Shapes of the first three modes of the building models in the elastic range

in all the building models, the models are classified as TS systems in this study. Further discussions can be found in references [16], [23] and [24].

3.2 Ground motion data

In this study, the seismic excitation was considered to be bidirectional in the X–Y plane, and three sets of artificial ground motions were generated. Note that the three sets of artificial ground motions were the same as those used in the previous study [16].

The target elastic spectrum of the "major" components with 5% critical damping, ${}_pS_{A\xi}(T,0.05)$, determined from the Building Standard Law of Japan [25] considering soil conditions, is calculated as

$${}_pS_{A\xi}(T,0.05)=\begin{cases}4.8+45T \quad \mathrm{m/s^2} & :T\le 0.16\mathrm{s}\\ 12.0 & :0.16\mathrm{s}\le T\le 0.576\mathrm{s}\\ 12.0(0.576/T) & :T\ge 0.576\mathrm{s}\end{cases}, \tag{29}$$

where T represents the natural period of the SDOF model.

The target spectrum of the "minor" components ${}_pS_{A\zeta}(T,0.05)$ is reduced by the parameter γ. Here, the parameter γ is set to 0, 0.5, 0.7, and 1.0; the ground motion is considered unidirectional for $\gamma=0$ whereas the spectra of the two horizontal components are identical when $\gamma=1.0$, as is assumed for the prediction of the largest peak response. According to López et al. [26], this ratio varies between 0.63 and 0.81 and the average ratio is 0.70. Therefore, the case $\gamma=0.7$ may be considered the most realistic case for real ground motion.

The phase angle is given by uniform random values and the Jenning type envelope function $e(t)$ proposed by the Building Centre of Japan:

$$e(t)=\begin{cases}(t/5)^2 & :0\text{s}\le t\le 5\text{s}\\ 1 & :5\text{s}\le t\le 35\text{s}\\ \exp\{-0.027(t-35)\} & :35\text{s}\le t\le 120\text{s}\end{cases}. \quad (30)$$

Figure 8 shows the elastic response spectra of artificial ground motions with 5% critical damping.

4 APPLICABILITY OF THE SIMPLIFIED PROCEDURE TO AN ASYMMETRIC BUILDING WITH BUCKLING-RESTRAINED BRACES

4.1 Prediction of the peak response

4.1.1. Prediction of the peak response of the first and second mode responses

Figure 9 shows the prediction of the peak response of the first and second mode responses employing equivalent linearization. It is seen that the intersection points of the capacity curve and demand curve represent the predicted peak response. Figure 10 shows the relationship of equivalent damping versus the equivalent displacement of the first and second modes for each model. The dots "●" in the figure represent the predicted peak responses of the first and second modes.

Figure 10 (a) shows that the equivalent damping ratios of the first and second modes at the predicted peak, h_{1eq} and h_{2eq}, respectively, are very close in the case of the asymmetric building model without BRBs (Model-O): h_{1eq} = 0.091 and h_{2eq} = 0.094. In contrast, the trends of the equivalent damping ratios of the two modes at the predicted peak are different for each model in the case of the asymmetric building model with BRBs. In the case of Model-BRB1L and BRB2L (Figure 10 (b) and (d)), h_{1eq} is larger than h_{2eq}; in case of Model-BRB1L, h_{1eq} = 0.130 and h_{2eq} = 0.094; while in the case of Model-BRB2L, h_{1eq} = 0.144 and h_{2eq} = 0.104. Meanwhile, h_{1eq} is smaller than h_{2eq} in the case of Model-BRB1H (Figure 10 (c)), and h_{1eq} is very close to h_{2eq} in the case of Model-BRB2H (Figure 10 (e)); in case of Model-BRB1H, h_{1eq} = 0.104 and h_{2eq} = 0.130, while in case of Model-BRB2H, h_{1eq} = 0.122 and h_{2eq} = 0.115.

4.1.2. Change in mode shape based on pushover analysis results

To evaluate the change in mode shape, the principal direction and torsional index based on mode shape for the first three modes were investigated using the pushover analyses results obtained in Step 2. The second and third modes at loading step n, ${}_n\boldsymbol{\varphi}_2$ and ${}_n\boldsymbol{\varphi}_3$ respectively, were calculated in terms of the displacement vector at loading step n, ${}_n\mathbf{d}$, and the second and

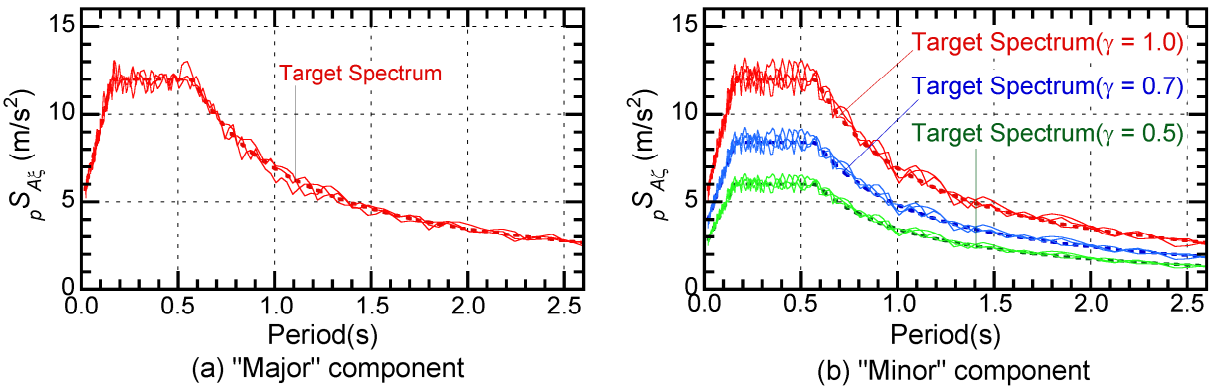

Figure 8: Elastic pseudo acceleration response spectra for simulated ground motion

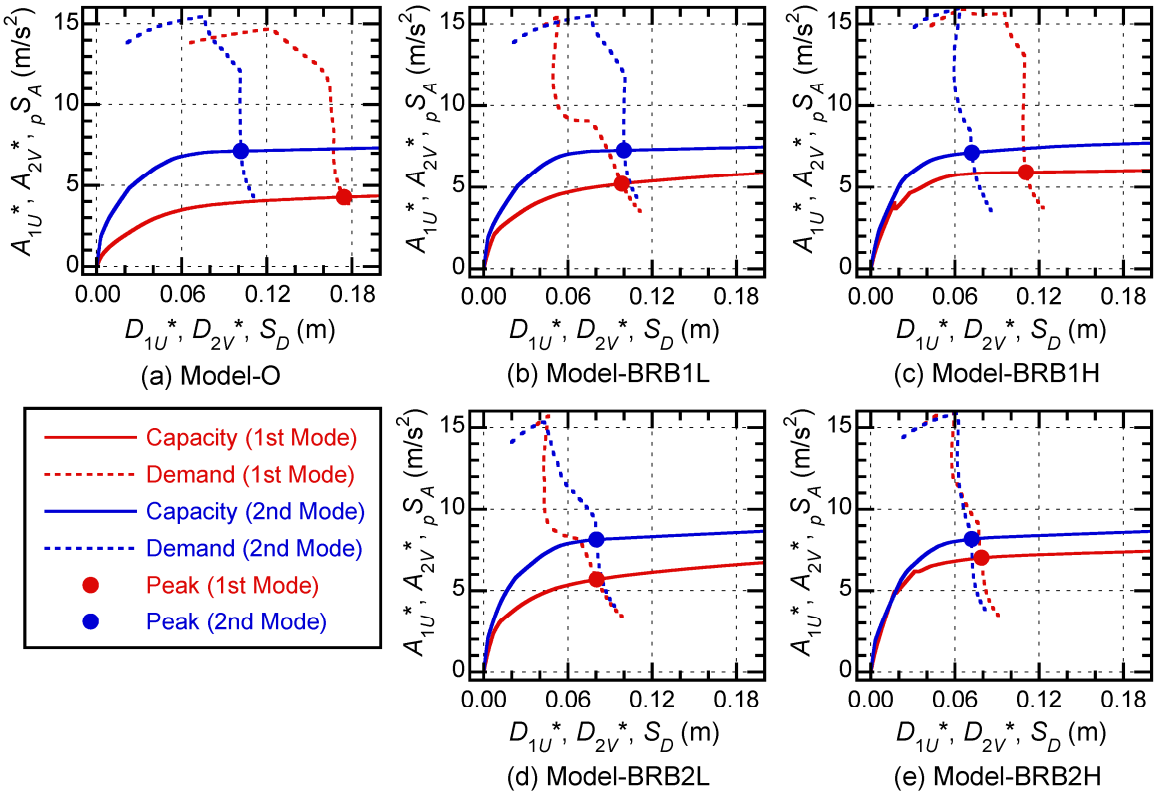

Figure 9: Prediction of the peak response of equivalent SDOF models

third mode vectors in the elastic range, $\boldsymbol{\varphi}_{2e}$ and $\boldsymbol{\varphi}_{3e}$ respectively, as

$$ {}_n\boldsymbol{\varphi}_2 = \boldsymbol{\varphi}_{2e} - \frac{\boldsymbol{\varphi}_{2e}^{\mathrm{T}}\mathbf{M}_n\boldsymbol{\varphi}_1}{{}_n\boldsymbol{\varphi}_1^{\mathrm{T}}\mathbf{M}_n\boldsymbol{\varphi}_1}\,{}_n\boldsymbol{\varphi}_1 = \boldsymbol{\varphi}_{2e} - \frac{\boldsymbol{\varphi}_{2e}^{\mathrm{T}}\mathbf{M}_n\mathbf{d}}{{}_n\mathbf{d}^{\mathrm{T}}\mathbf{M}_n\mathbf{d}}\,{}_n\mathbf{d}, \tag{31} $$

$$ {}_n\boldsymbol{\varphi}_3 = \boldsymbol{\varphi}_{3e} - \frac{\boldsymbol{\varphi}_{3e}^{\mathrm{T}}\mathbf{M}_n\boldsymbol{\varphi}_1}{{}_n\boldsymbol{\varphi}_1^{\mathrm{T}}\mathbf{M}_n\boldsymbol{\varphi}_1}\,{}_n\boldsymbol{\varphi}_1 - \frac{\boldsymbol{\varphi}_{3e}^{\mathrm{T}}\mathbf{M}_n\boldsymbol{\varphi}_2}{{}_n\boldsymbol{\varphi}_2^{\mathrm{T}}\mathbf{M}_n\boldsymbol{\varphi}_2}\,{}_n\boldsymbol{\varphi}_2 = \boldsymbol{\varphi}_{3e} - \frac{\boldsymbol{\varphi}_{3e}^{\mathrm{T}}\mathbf{M}_n\mathbf{d}}{{}_n\mathbf{d}^{\mathrm{T}}\mathbf{M}_n\mathbf{d}}\,{}_n\mathbf{d} - \frac{\boldsymbol{\varphi}_{3e}^{\mathrm{T}}\mathbf{M}_n\boldsymbol{\varphi}_2}{{}_n\boldsymbol{\varphi}_2^{\mathrm{T}}\mathbf{M}_n\boldsymbol{\varphi}_2}\,{}_n\boldsymbol{\varphi}_2 . \tag{32} $$

Next, the tangent of the angle of the principal direction of the ith mode at loading step n, $\tan {}_n\psi_i$, and the torsional index of the ith mode at loading step n, ${}_nR_{\rho i}$, were calculated as

$$ \tan {}_n\psi_i = -\sum_j m_j\,{}_n\phi_{Yji} \Big/ \sum_j m_j\,{}_n\phi_{Xji}\,, \tag{33} $$

$$ {}_nR_{\rho i} = \sqrt{\sum_j I_j\,{}_n\phi_{\Theta ji}^{\,2} \Big/ \left(\sum_j m_j\,{}_n\phi_{Xji}^{\,2} + \sum_j m_j\,{}_n\phi_{Yji}^{\,2} \right)}\,. \tag{34} $$

Figure 11 shows the changes in ${}_n\psi_i$ and ${}_nR_{\rho i}$ at each loading step for all building models. The dots "●" in this figure correspond to the points of the predicted peak response of the first mode.

Figure 11(a) shows that the changes in ${}_n\psi_i$ and ${}_nR_{\rho i}$ are very small in the case of Model-O. In contrast, the changes in ${}_n\psi_i$ and ${}_nR_{\rho i}$ are small in the case of Model-BRB1L and BRB2L (Figure 11 (b) and (d), respectively), and significant in the case of Model-BRB1H and BRB2H (Figure 11 (c) and (e), respectively); in particular, in the case of Model-BRB1H, the

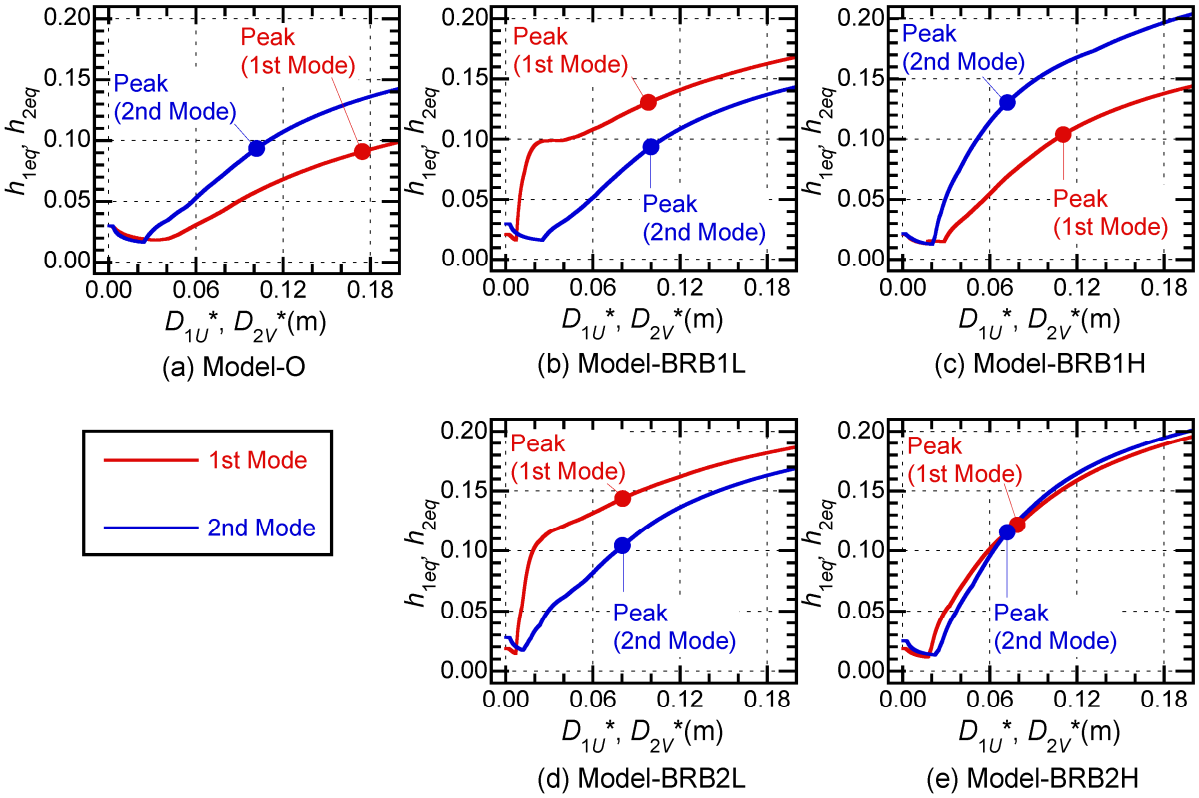

Figure 10: Equivalent damping ratio–equivalent displacement relationship of equivalent SDOF models

change in ${}_n\psi_i$ is about 50° from the elastic stage ($\psi_{1e} = 50.6^\circ$) to the predicted peak response ($\psi_1 = 2.2^\circ$). Figure 11 (c) and (e) shows that ${}_nR_{\rho 1}$ and ${}_nR_{\rho 2}$ decrease as ${}_nR_{\rho 3}$ increases rapidly as the equivalent displacement ${}_nD_1{}^*$ increases, in the case of Model-BRB1H and Model-BRB2H. This implies that the first two modes become almost purely translational modes when the building models respond in the nonlinear range.

4.2 Comparisons of the predicted results with the results of time-history analyses

4.2.1. Time-history analysis cases

The applicability of the simplified procedure to asymmetric buildings with BRBs was evaluated as follows. First, nonlinear dynamic (time-history) analyses were carried out for fixed values of γ, various spectral ratios of "minor" to "major" components (γ = 0, 0.5, 0.7, and 1.0) and various directions of the incidence of seismic input. Then, from the results of each set of artificial ground motions, the envelope of the peak response of various directions of incidence was obtained for the cases γ = 0, 0.5, 0.7, while for the case γ = 1.0, the average of the peak response in directions of incidence was obtained. Finally, the averages of the results for the three sets of artificial ground motions were compared with the predicted "largest" peak response. Note that the angle of incidence of the "major" component with respect to the X-axis, ψ, varied at 15° intervals from $(\psi_1 - 90)^\circ$ to $(\psi_1 + 90)^\circ$, where ψ_1 is the angle of incidence of the U-axis corresponding to the predicted peak equivalent displacement of the first mode, $D_{1U}{}^*{}_{\max}$, shown in Figure 11. Therefore, $4 \times 3 \times 13 = 156$ cases were considered for the nonlinear time-history analyses of each building model.

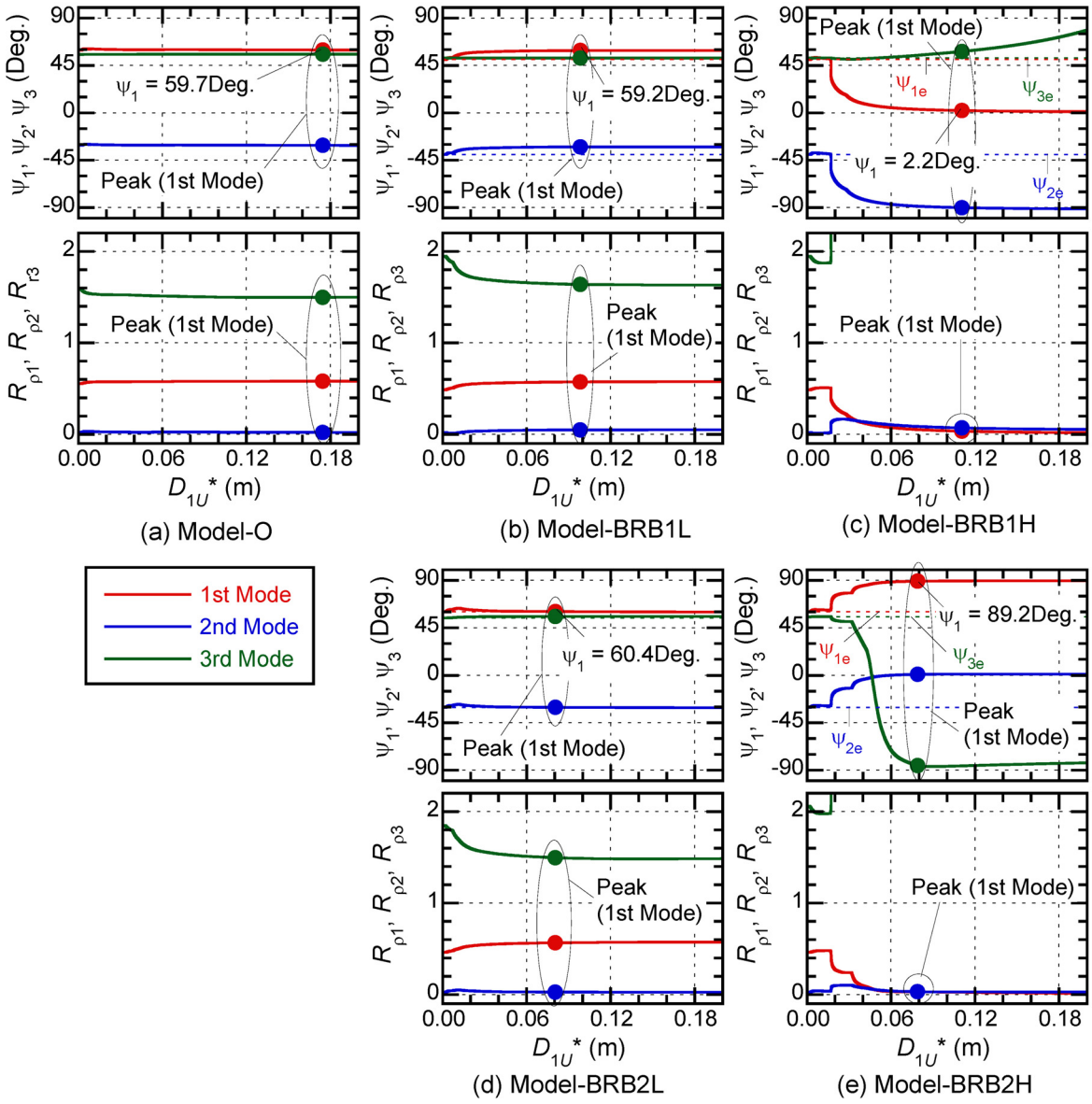

Figure 11: Change in the principal direction of modal responses and torsional indices in the nonlinear stage evaluated by pushover analysis

4.2.2. Accuracy of the results predicted using the simplified procedure

Figure 12 compares the peak displacement at the roof obtained from dynamic analysis results and the predicted peak response for each building model. In this figure, the plot "Envelope" for the cases γ = 0, 0.5 and 0.7 shows the average of the envelope of three sets of artificial ground motions (for each set, 13 directions are considered) for each γ, while the plot "Ave. (γ = 1.0)" indicates the average of 36 cases (three sets of artificial ground motions × 12 directions) of the results for γ = 1.0.

In the case of Model-O, as shown in Figure 12 (a), the predicted results approximate the upper bound of the dynamic analysis results in the X-direction, while in the Y-direction, the predicted results are conservative relative to the time-history analysis results except for Frame X1. In the case of building models with BRBs, the trends strongly depend on each model; in the cases of Model-BRB1L (Figure 12 (b)), BRB1H (Figure 12 (c)) and BRB2H (Figure 12

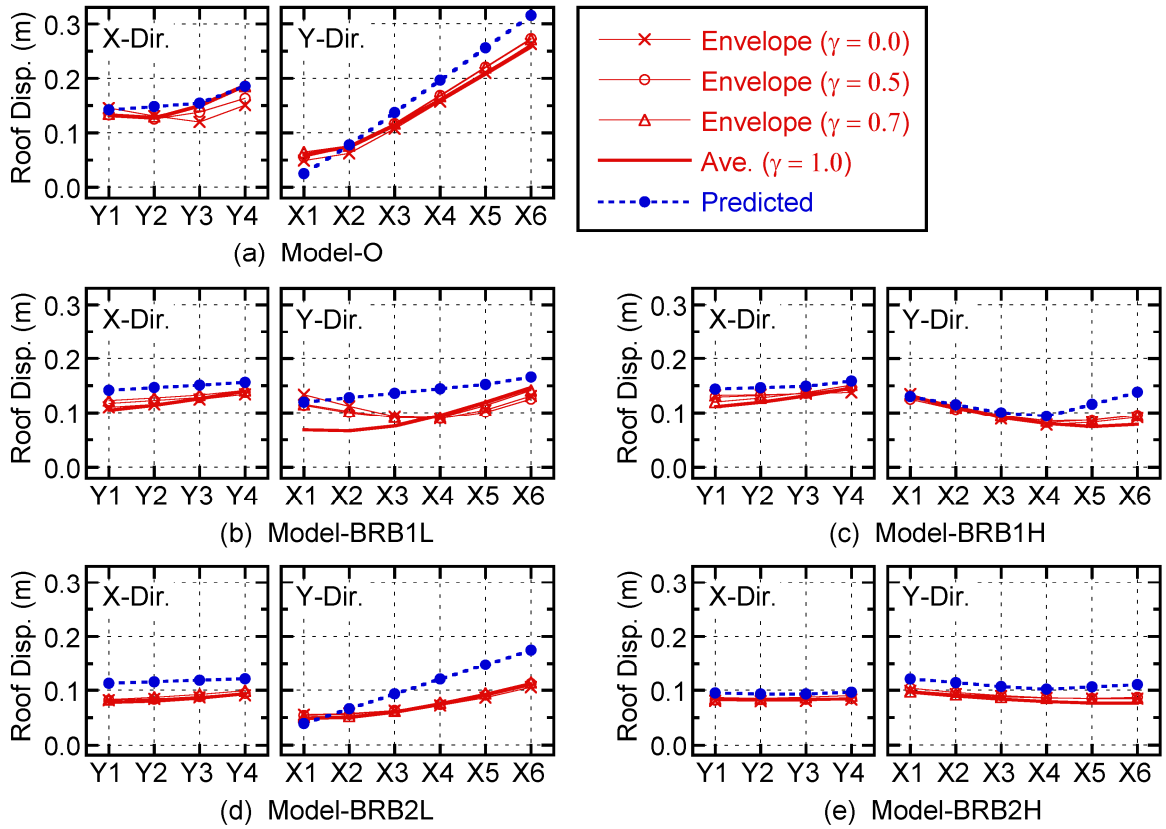

Figure 12: Prediction of "the largest" peak displacement at roof and comparisons with dynamic analyses results

(e)), the predicted results approximate the upper bound of the dynamic analysis results of all frames, while trends similar to those seen in Figure 12 (a) are observed in the case of Model-BRB2L (Figure 12 (d)).

Figure 13 compares the peak storey drift at edge frames (Frames Y1, Y4, X1 and X6) obtained from time-history analyses and the predicted peak response for each building model. As shown in this figure, the predicted results satisfactorily agree with the dynamic analysis results of all models, except Frame X1 of Model-O (Figure 13(a)) and BRB2L (Figure 13(d)). According to these results, the simplified procedure presented in reference [16] may be applicable to asymmetric buildings with BRBs.

Figure 14 shows the effect of the direction of incidence of the "major" component on the peak roof displacement at edge frames (Frames Y1, Y4, X1 and X6). In this figure, the "normalized displacement" indicates the peak roof displacement in various directions for $\gamma = 0$, 0.5 and 0.7 divided by the average for $\gamma = 1.0$.

Also shown is the predicted peak response, and ψ_{1e} and ψ_1, the angles of incidence of the principal direction of the first modal response with respect to the X-axis, in the elastic range and corresponding to $D_{1U}{}^{*}{}_{\max}$, respectively.

Figure 14(a) shows that, in the case of Model-O and for $\gamma = 0$, 0.5 and 0.7, the normalized displacement at edge frames is less than 1 in most cases, as expected. This point is important because it is assumed the ratio γ equals 1.0 in the simplified procedure for the prediction of the "largest" peak response. In Frame X6, the flexible edge frame in the Y-direction, the normalized displacement is the largest and close to 1.0 when ψ is close to ψ_1. However, as is seen in Figures 14(b) to (e), the trend strongly depends on the building model; trends similar

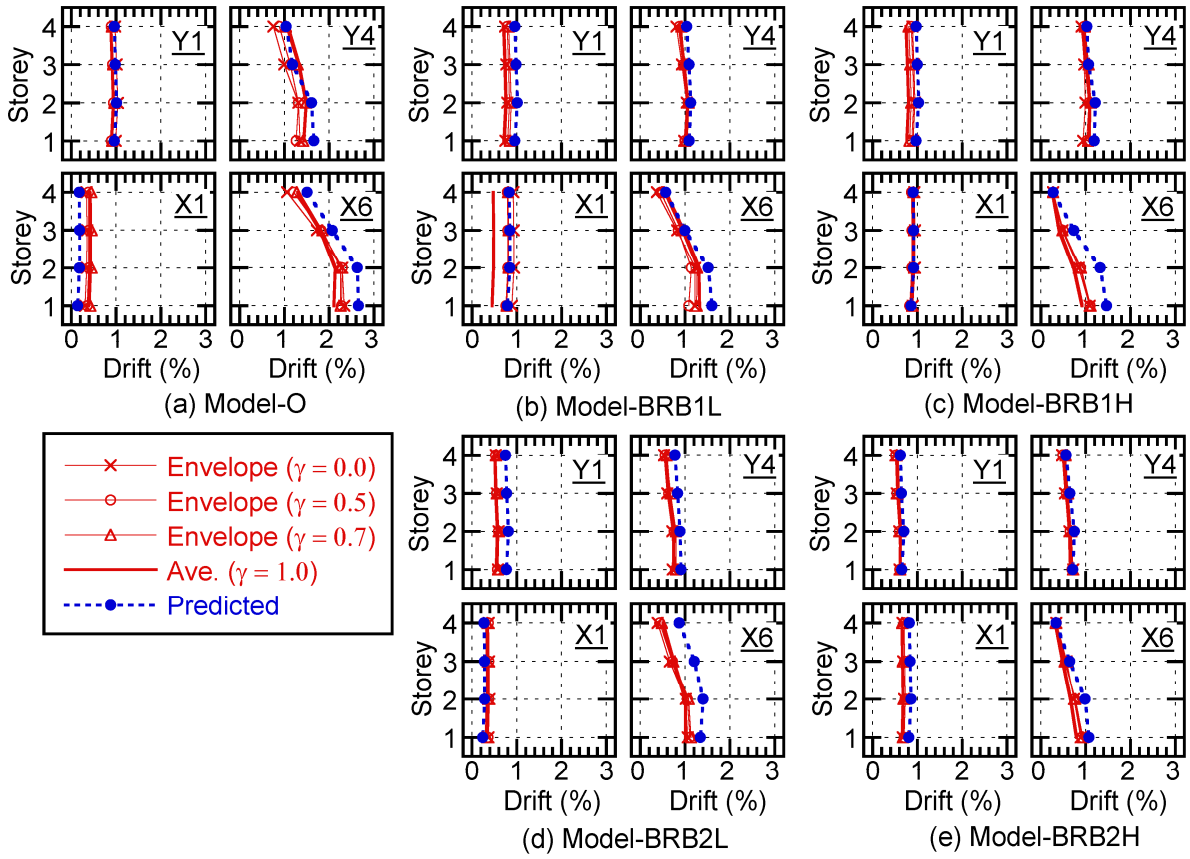

Figure 13: Prediction of "the largest" peak storey drift at edge frames (frames Y1, Y4, X1 and X6) and comparisons with dynamic analysis results

to those for Model-O are observed for Model-BRB1L and BRB2L (Figures 14(b) and (d), respectively) except for Frame X1 of Model-BRB1L, the normalized displacement of which is much larger than 1 in some cases. By contrast, in the case of Model-BRB1H (Figure 14(c)), the normalized displacement of Frame Y4, where the largest roof displacement occurs in this building model, is the largest and close to 1.0 when ψ is close to ψ_1, not ψ_{1e}. Meanwhile, in the case of Model-BRB2H (Figure 14(e)), the normalized displacement of Frame X1, where the largest roof displacement occurs in this building model, is the largest and close to 1.0 when ψ is close to ψ_1, not ψ_{1e}. These results imply that the most critical direction of incidence of the seismic input is different from that in the elastic range, in the case of asymmetric buildings with BRBs responding beyond the elastic range.

5 EFFECT OF THE CHANGE IN MODE SHAPE ON THE ACCURACY OF THE NONLINEAR STATIC PROCEDURE

5.1 Prediction cases

In the simplified procedure presented in reference [16], there are two main differences from conventional pushover analyses [10–13]. One is that the change in the mode shape in nonlinear range is considered, and the other is that the combination of two modal responses is considered by the force distributions used in pushover analyses for the prediction of peak responses (referred to as the envelope method). In contrast, especially in modal pushover analy-

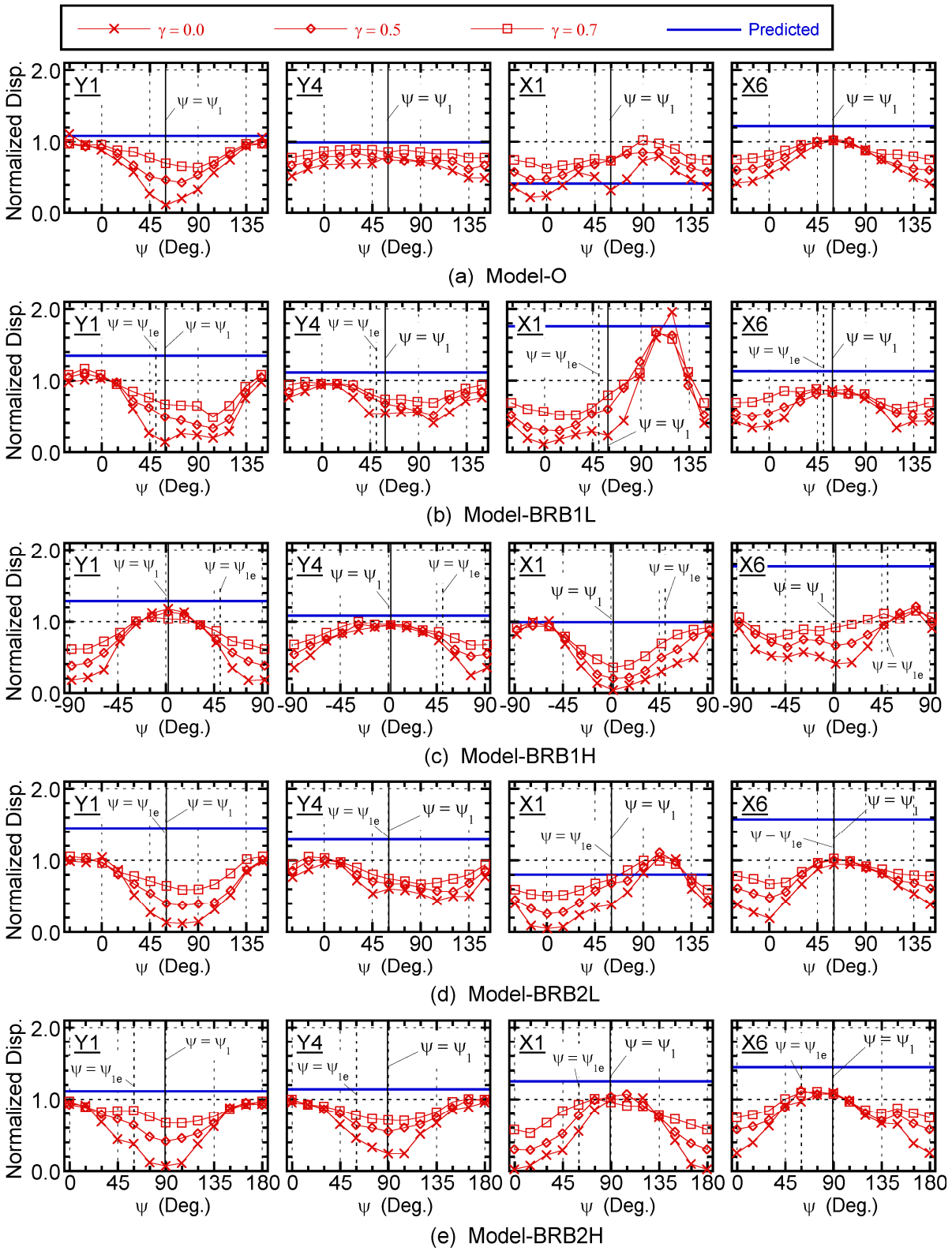

Figure 14: Effect of the direction of incidence of the "major" component on the peak roof displacement at edge frames (Frames Y1, Y4, X1 and X6)

sis in [13], the mode shape is assumed as that in the elastic range, and the square root of the sum of squares (SRSS) rule or CQC rule is applied as the combination rule.

In this section, the effects of the change in mode shape and the combination rule on the accuracy of the NSP for asymmetric buildings with BRBs are investigated.

The parameters in the prediction cases are (i) consideration of the change in mode shape (variant/invariant) and (ii) the combination rules (envelope method/SRSS method).

5.1.1. Parameter (i): consideration of the change in mode shape

In the case of the "invariant" mode shape, pushover analyses in Steps 1 and 3 are based on invariant force distributions; force distributions used in Steps 1 and 3, $\mathbf{P_{1e}}$ and $\mathbf{P_{2e}}$ respectively, are calculated as

$$\mathbf{P_{1e}} = \mathbf{M}\left(\Gamma_{1Ue}\boldsymbol{\varphi}_{\mathbf{1e}}\right), \mathbf{P_{2e}} = \mathbf{M}\left(\Gamma_{2Ve}\boldsymbol{\varphi}_{\mathbf{2e}}\right). \tag{35}$$

From the displacement vector at loading step n, ${}_n\mathbf{d}$, the equivalent displacement and acceleration of the first mode, ${}_nD_{1Ue}{}^*$ and ${}_nA_{1Ue}{}^*$ respectively, and those of the second mode, ${}_nD_{2Ve}{}^*$ and ${}_nA_{2Ve}{}^*$ respectively, are calculated as

$${}_nD_{1Ue}{}^* = \Gamma_{1Ue}\boldsymbol{\varphi}_{\mathbf{1e}}{}^{\mathbf{T}}\mathbf{M}\,{}_n\mathbf{d}/M_{1Ue}{}^*, {}_nA_{1Ue}{}^* = \Gamma_{1Ue}\boldsymbol{\varphi}_{\mathbf{1e}}{}^{\mathbf{T}}\,{}_n\mathbf{f_R}/M_{1Ue}{}^*, \tag{36}$$

$${}_nD_{2Ve}{}^* = \Gamma_{2Ve}\boldsymbol{\varphi}_{\mathbf{2e}}{}^{\mathbf{T}}\mathbf{M}\,{}_n\mathbf{d}/M_{2Ve}{}^*, {}_nA_{2Ve}{}^* = \Gamma_{2Ve}\boldsymbol{\varphi}_{\mathbf{2e}}{}^{\mathbf{T}}\,{}_n\mathbf{f_R}/M_{2Ve}{}^*, \tag{37}$$

where

$$M_{1Ue}{}^* = \Gamma_{1Ue}{}^2\boldsymbol{\varphi}_{\mathbf{1e}}{}^{\mathbf{T}}\mathbf{M}\boldsymbol{\varphi}_{\mathbf{1e}}, M_{2Ve}{}^* = \Gamma_{2Ve}{}^2\boldsymbol{\varphi}_{\mathbf{2e}}{}^{\mathbf{T}}\mathbf{M}\boldsymbol{\varphi}_{\mathbf{2e}}, \tag{38}$$

$$\Gamma_{1Ue} = \frac{\boldsymbol{\varphi}_{\mathbf{1e}}{}^{\mathbf{T}}\mathbf{M}\boldsymbol{\alpha}_{\mathbf{Ue}}}{\boldsymbol{\varphi}_{\mathbf{1e}}{}^{\mathbf{T}}\mathbf{M}\boldsymbol{\varphi}_{\mathbf{1e}}}, \Gamma_{2Ve} = \frac{\boldsymbol{\varphi}_{\mathbf{2e}}{}^{\mathbf{T}}\mathbf{M}\boldsymbol{\alpha}_{\mathbf{Ve}}}{\boldsymbol{\varphi}_{\mathbf{2e}}{}^{\mathbf{T}}\mathbf{M}\boldsymbol{\varphi}_{\mathbf{2e}}}, \tag{39}$$

$$\begin{cases} \boldsymbol{\alpha}_{\mathbf{Ue}} = \{\cos\psi_{1e} \quad \cdots \quad \cos\psi_{1e} \quad -\sin\psi_{1e} \quad \cdots \quad -\sin\psi_{1e} \quad 0 \quad \cdots \quad 0\}^{\mathbf{T}} \\ \boldsymbol{\alpha}_{\mathbf{Ve}} = \{\sin\psi_{1e} \quad \cdots \quad \sin\psi_{1e} \quad \cos\psi_{1e} \quad \cdots \quad \cos\psi_{1e} \quad 0 \quad \cdots \quad 0\}^{\mathbf{T}} \end{cases}. \tag{40}$$

The peak equivalent displacement and acceleration of the first and second models are predicted from the ${}_nA_{1Ue}{}^*-{}_nD_{1Ue}{}^*$ curve and ${}_nA_{2Ve}{}^*-{}_nD_{2Ve}{}^*$ curve, respectively.

In the case of the "variant" mode shape, pushover analyses in Steps 1 and 3 are carried out according to section 2.

5.1.2. Parameter (ii): combination rule

In the case of the envelope method, the peak response at each frame in Step 5 is predicted according to section 2.5. Note that, in the case of the invariant mode shape, Eq. (23) is rewritten considering the elastic mode shapes instead of inelastic mode shapes at peak response:

$$\begin{cases} \mathbf{P_{Ue}}^{\pm} = \mathbf{M}\left(\Gamma_{1Ue}\boldsymbol{\varphi}_{\mathbf{1e}}A_{1Ue}{}^*{}_{\max} \pm 0.5\Gamma_{2Ve}\boldsymbol{\varphi}_{\mathbf{2e}}A_{2Ve}{}^*{}_{\max}\right) \\ \mathbf{P_{Ve}}^{\pm} = \mathbf{M}\left(\pm 0.5\Gamma_{1Ue}\boldsymbol{\varphi}_{\mathbf{1e}}A_{1Ue}{}^*{}_{\max} + \Gamma_{2Ve}\boldsymbol{\varphi}_{\mathbf{2e}}A_{2Ve}{}^*{}_{\max}\right) \end{cases}. \tag{41}$$

In the case of the SRSS method, the peak response at each frame in Step 5 is predicted from the SRSS rule as follows. Let $d_{Xmj1U\max}$ and $d_{Ynj1U\max}$ be the peak displacement of the mth frame in the X-direction and nth frame in the Y-direction at the jth floor, respectively, obtained from the first mode response in Step 1, while $d_{Xmj2V\max}$ and $d_{Ynj2V\max}$ are those obtained from the second mode response in Step 3. The peak displacement of the mth frame in the X-direction at the jth floor, $d_{Xmj\max}$, and nth frame in the Y-direction at the jth floor, $d_{Yn\max}$, are calculated according to

$$d_{Xmj\max} = \sqrt{d_{Xmj1U\max}{}^2 + d_{Xmj2V\max}{}^2}, d_{Ynj\max} = \sqrt{d_{Ynj1U\max}{}^2 + d_{Ynj2V\max}{}^2} . \quad (42)$$

5.2 Comparisons of the predicted results

5.2.1. Comparisons of peak roof displacement

Figure 15 compares the peak displacement at the roof obtained from dynamic analyses and the predicted peak response in the case of the envelope method. Figure 15(a) reveals that the difference in the predicted results using invariant and variant mode shapes is negligibly small in the case of Model-O. This is because, as shown in Figure 11(a), the change in the first mode shape is very small. In contrast, the effect of the consideration of the change in mode shapes on the accuracy of the predicted results strongly depends on the building model, in the case of asymmetric building models with BRBs in this study; in the case of Model-BRB1L and BRB2L (Figures 15(b) and (d), respectively), the difference in the predicted results is very small, while it is significant in the case of Model-BRB1H (Figure 15(c)), and moderate in the case of Model-BRB2H (Figure 15(e)).

Note that in the case of Model-BRB1H, the results predicted from the variant mode shape are closer than those predicted from the invariant mode shape to the dynamic analysis results except for Frames X5 and X6. In the case of Model-BRB2H, the predicted peak response at Frame X1 obtained from the invariant mode shape is unconservative in comparison with the dynamic analysis results, while the predicted response obtained from the variant mode shape agrees satisfactorily with the dynamic analysis results. Therefore, the predicted peak responses obtained from the variant mode shape are more accurate than those obtained from the in-

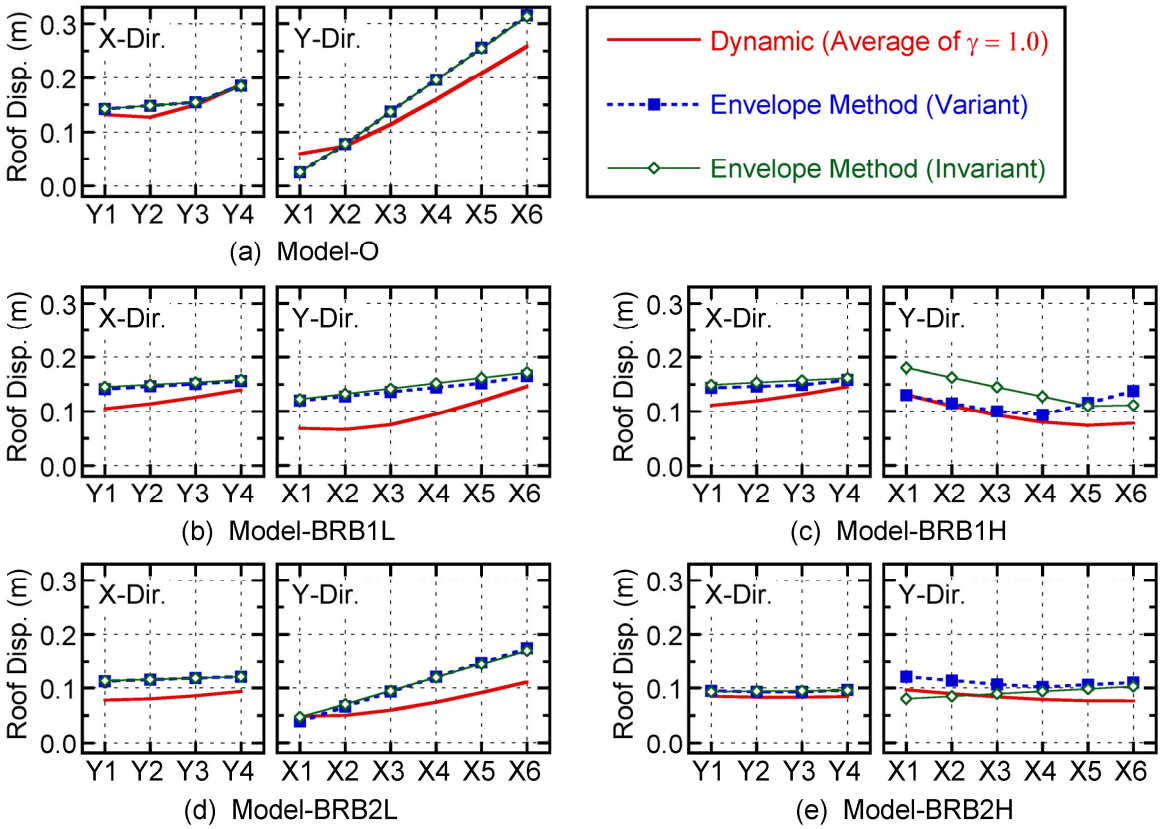

Figure 15: Comparisons of the peak response predicted from variant and invariant mode shapes and dynamic analysis results (envelope method)

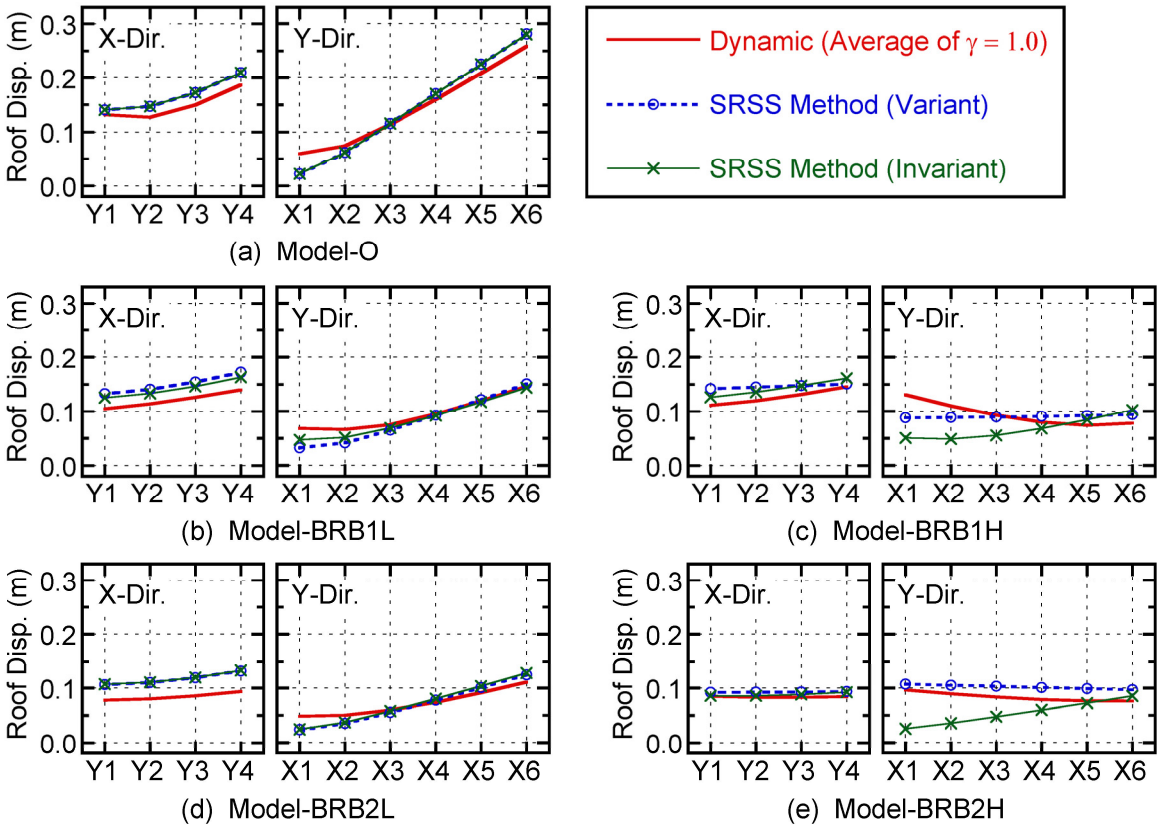

Figure 16: Comparisons of predicted peak response using "variant" and "invariant" mode shapes and dynamic analyses results (SRSS method)

variant mode shape.

Figure 16 compares the peak displacement at the roof obtained from dynamic analyses and the predicted peak response in the case of the SRSS method. It is seen that the predicted peak responses are less conservative than those in the case of the envelope method shown in Figure 15. As shown in Figures 16 (a), (b) and (d), the differences in the prediction results obtained with invariant and variant mode shapes are negligibly small in the cases of Model-O, Model-BRB1L, and Model-BRB2L, and these predicted results agree well with the dynamic analysis results except for Frame X1. In contrast, the accuracy of the results predicted with invariant mode shapes is very poor in case of Model-BRB1H (Figure 16 (c)) and Model-BRB2H (Figure 16 (e)), while the results predicted with the variant mode shape are closer to the dynamic analysis results; however, in the case of Model-BRB1H, the predicted peak displacement at Frame X1 is unconservative in comparison with the dynamic analysis results, even if the change in mode shape in the nonlinear stage is considered.

5.2.2. Comparisons of the amplification of roof displacement

To evaluate the amplification of displacement due to the unfavourable torsional effect, the normalized roof displacement, which is defined as the ratio of the displacement at each frame to that of the centre of mass, has been studied often (e.g., [11] and [12]). Figure 17 compares the normalized roof displacement obtained from dynamic analysis results (average for $\gamma = 1.0$) and results predicted employing two methods (i.e., the envelope method and SRSS method) and using the variant mode shape.

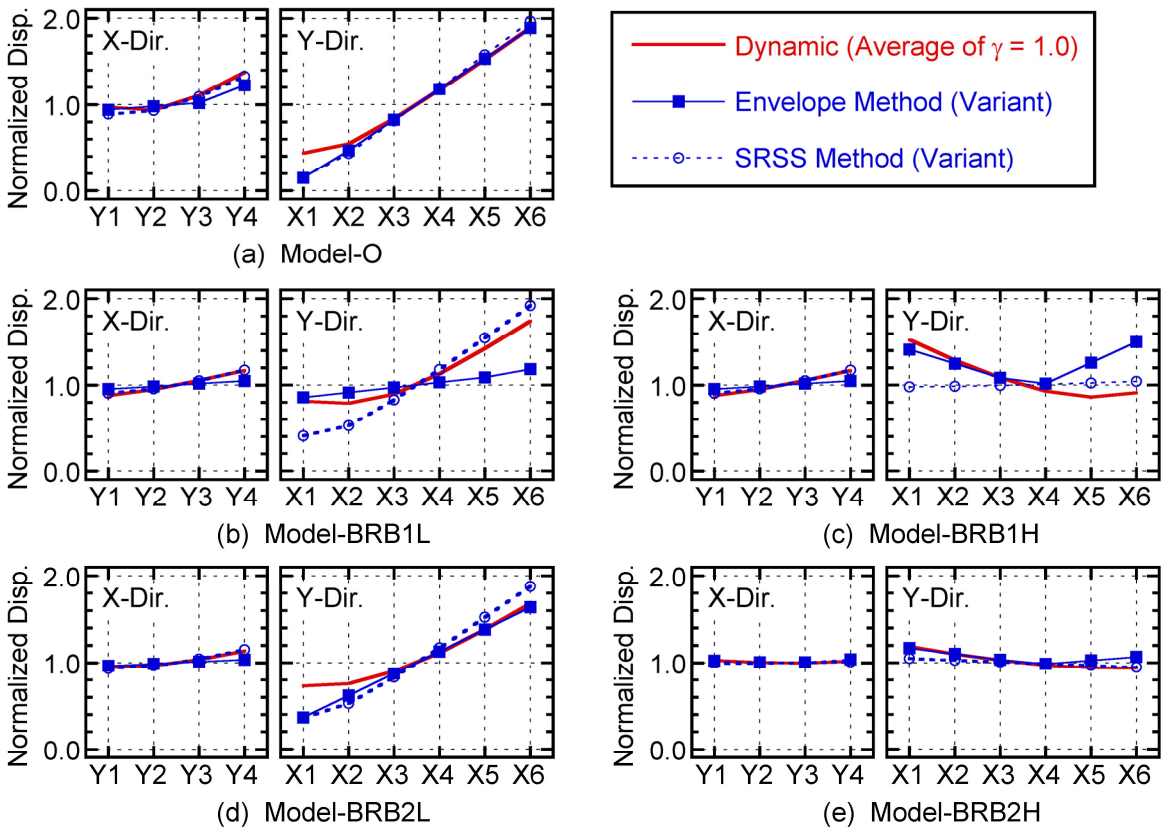

Figure 17: Comparisons of normalized roof displacement with dynamic analysis and results predicted using the envelope method and SRSS method (variant mode shape)

In the case of Model-O (Figure 17(a)), the differences in results predicted with the two methods are negligible and the results agree well with the dynamic analysis results, except for Frame X1.

However, the trends of the asymmetric building models with BRBs strongly depend on the model. In the case of Model-BRB1L (Figure 17(b)), the differences in results predicted with the envelope method and SRSS method are notable; the normalized displacement at Frame X6 obtained using the envelope method is smaller than the dynamic analysis result, while that obtained using the SRSS method agrees well with the dynamic analysis result. By contrast, in the case of Model-BRB1H (Figure 17(c)), the normalized displacement obtained using the envelope method agrees well with the dynamic analysis results for Frame X1, while the results obtained using the SRSS method fail to fit the dynamic analysis results. The trends of Model-BRB2L (Figure 17(d)) are similar to those of Model-O. In the case of Model-BRB2H (Figure 17(e)), the results predicted using the envelope method fit the dynamic analysis results for all frames, while the normalized displacement at Frame X1 obtained using the SRSS method is lower than the dynamic analysis result.

Note that the centre of mass at the roof is *not* the reference point for pushover analysis in the envelope method, which is one of the largest differences from other pushover-based simplified procedures (e.g., [14]). Therefore, underestimation of the amplification ratio due to the torsional effect at the flexible/weak side frame itself does not directory lead to underestimation of the peak displacement at the flexible/weak side frame in this simplified procedure [16], as is seen for the case of Model-BRB1L in Figure 15 (c).

Figure 18 compares the normalized roof displacement obtained from dynamic analyses and predicted using the two methods and the invariant mode shape. Trends similar to those in Fig-

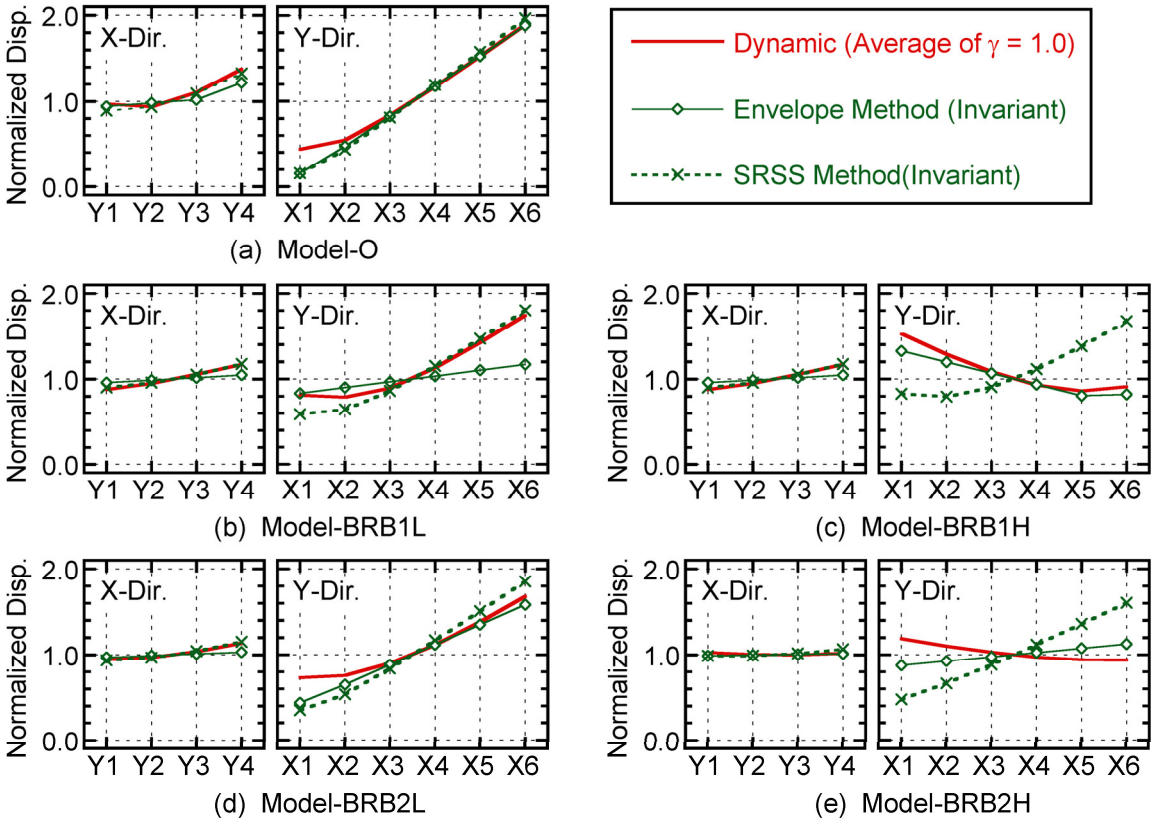

Figure 18: Comparisons of normalized roof displacement with dynamic analysis and results predicted using the envelope method and SRSS method (invariant mode shape)

ure 17 are seen in the case of Model-O (Figure 18(a)), Model-BRB1L (Figure 18(b)), and BRB2L (Figure 18(d)). However, in case of Model-BRB1H (Figure 18(c)) and Model-BRB2H (Figure 18(e)), the results predicted using the invariant mode shape fail to fit the dynamic analysis results. In particular, the results predicted using the SRSS method fail to show the frames in which the largest displacement occurs; as shown in Figures 18(c) and (e), the normalized displacement obtained from dynamic analyses is largest at Frame X1, while that predicted using the SRSS method is largest at Frame X6. Similarly, inaccurate prediction due to the assumption of the invariant mode shape has been pointed out by Isakovic and Fischinger in the case of bridge structures [27]. Although the normalized displacement predicted using the envelope method agrees well with the dynamic analysis results in the case of Model-BRB1H (Figure 18(c)), it fails to fit the dynamic analysis results in the case of Model-BRB2H (Figure 18(e)). Therefore, for the better prediction of peak displacement in each frame, the effect of the change in mode shape at each nonlinear stage should be properly considered.

5.2.3. Comparisons of the properties of equivalent SDOF models

To investigate the effect of the change in mode shape in each nonlinear stage on the properties of equivalent SDOF models, Figures 19 and 20 compare the equivalent acceleration–equivalent displacement curve and the equivalent damping–equivalent displacement curve of Model-O, Model-BRB1L, and Model-BRB1H. The figures show that the differences in properties of equivalent SDOF models are (a) negligible for Model-O, (b) small for Model-BRB1L, and (c) notable for Model-BRB1H. In particular, for Model-BRB1H, the peak response of the first mode predicted using the invariant mode shape is smaller than that predicted using the variable mode shape, because the equivalent damping obtained using the

invariant mode shape is significantly larger than that obtained using the variant mode shape (Figure 19(c)). In contrast, the peak response of the second mode predicted using the invariant mode shape is larger than that predicted using the variable mode shape (Figure 20(c)). These results may explain the difference in the predicted results shown in Figure 16 (c); i.e., the peak response predicted with the SRSS method and invariant mode shapes having poorer accuracy than that predicted with the variant mode shapes.

In conclusion, for a more accurate NSP, consideration of the change in mode shape in each nonlinear stage is essential in the case of asymmetric buildings with BRBs, and according to the combination rule, the envelope method may provide results that are more conservative than the SRSS rule applied in references [11–13].

6 CONCLUSIONS

The applicability of the simplified procedure previously proposed by the author [16] to four-storey RC asymmetric buildings with a hysteresis damper (BRB) was numerically investigated. The predicted largest peak response was compared with nonlinear dynamic (time-history) analysis results considering various directions of the incidence of the seismic input. Although the number of building models considered in the study was limited, the following primary findings were made.

1. The simplified procedure proposed by the author [16] is applicable to asymmetric buildings with BRBs that are classified as TS buildings. The predicted "largest" peak responses of all four asymmetric buildings with BRBs satisfactorily enveloped the results obtained in dynamic analyses.
2. The effect of the change in mode shape in each nonlinear stage on the accuracy of the NSP may be important in the case of asymmetric buildings with BRBs. In this study, there were cases in which the accuracy of the predictions based on an elastic mode shape was poor.
3. For the combination rule considering bidirectional excitation, the envelope method, which is one of the prediction steps in the simplified procedure [16], provides more conservative results than the SRSS method; the responses predicted with SRSS methods may be unconservative, especially when the change in the mode shape is not considered. Meanwhile, the response predicted using the envelope method satisfactorily approximates the envelope of dynamic analysis results.

Note that the discussions above focus only on TS asymmetric buildings. The author concluded in reference [24] that the applicability of the simplified procedure to a torsionally flexible (TF) asymmetric building is questionable. However, the applicability to TF asymmetric buildings with hysteresis dampers in outermost frames remains unknown. This is a problem that should be investigated in future work.

REFERENCES

[1] R. K. Goel, Effects of supplemental viscous damping on seismic response of asymmetric-plan systems, Earthquake Engineering and Structural Dynamics, **27**, 125-141, 1998.

[2] R. K. Goel, Seismic behaviour of asymmetric buildings with supplemental damping, Earthquake Engineering and Structural Dynamics, **29**, 461-480, 2000.

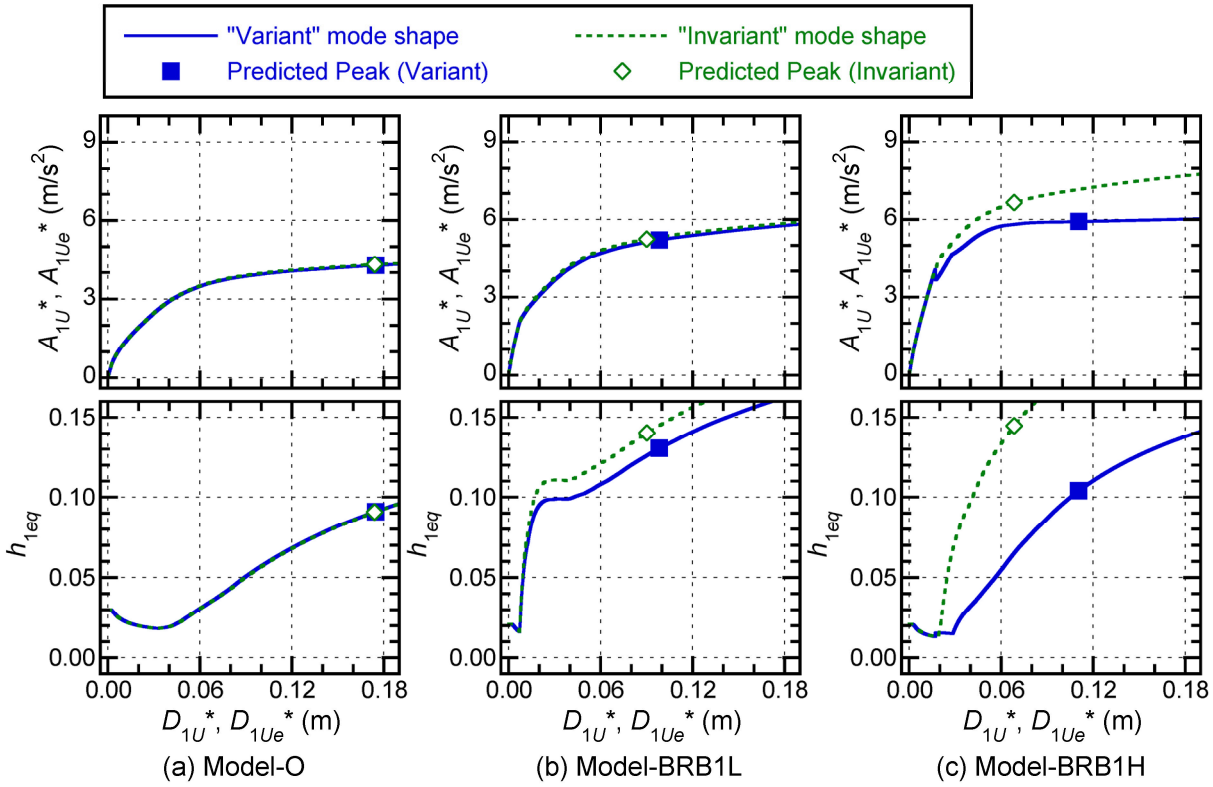

Figure 19: Comparisons of the properties of equivalent SDOF models (first mode)

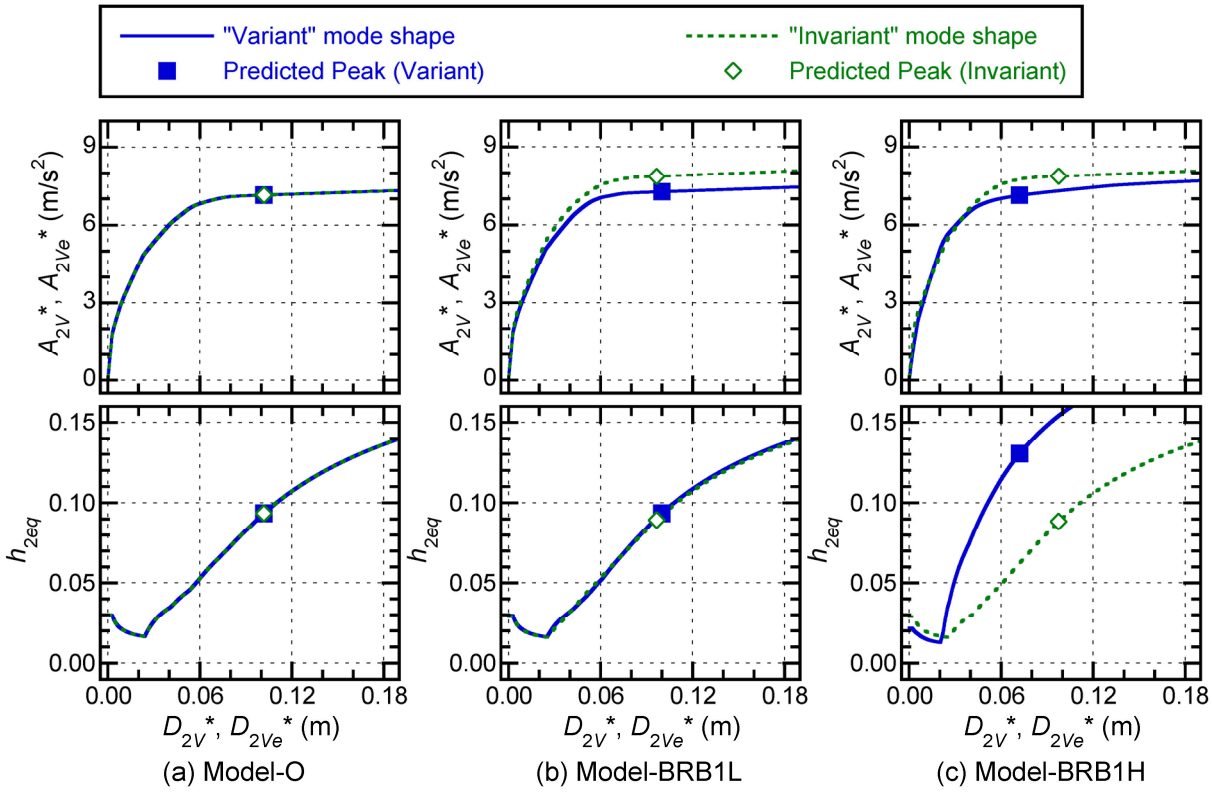

Figure 20: Comparisons of the properties of equivalent SDOF models (second mode)

[3] R. K. Goel and C. A. Booker, Effect of supplemental viscous damping on inelastic seismic response of asymmetric systems, Earthquake Engineering and Structural Dynamics, **30**, 411-430, 2001.

[4] W. Lin, and A. K. Chopra, Understanding and predicting effects of supplemental viscous damping on seismic response of asymmetric one-storey systems, Earthquake Engineering and Structural Dynamics, **30**, 1475-1474, 2001.

[5] L. Landi, P. P. Diotallevi and G. Castellari, On the Design of Viscous Dampers for the Rehabilitation of Plan-Asymmetric Buildings, Journal of Earthquake Engineering, **17**, 1141-1161, 2013.

[6] J. C. De la Llera, J. L. Almazán, and I. J. Vial, Torsional balance of plan-asymmetric structures with friction dampers: analytical results, Earthquake Engineering and Structural Dynamics, **34**, 1089-1108, 2005.

[7] F. Mazza, Displacement-based seismic design of hysteretic damped braces for retrofitting in-plan irregular r.c. framed structures, Soil Dynamics and Earthquake Engineering, **66**, 231-240, 2014.

[8] M. Saiidi, M. A. Sozen, Simple nonlinear seismic analysis of R/C structures, Journal of Structural Division, ASCE, **107**, 937–952, 1981.

[9] P. Fajfar, M. Fischinger, N2-a method for non-linear seismic analysis of regular buildings. In: Proceedings of ninth world conference on earthquake engineering, **5**, 111–116, Tokyo-Kyoto, Japan, 1988.

[10] P. Fajfar, D. Marusić, I. Perus, and G. Magliulo, The extension of The N2 method to asymmetric buildings, Proceedings of the Fourth Forum on Implications of Recent Earthquakes on Seismic Risk, Technical Report TIT/EERG 02/1, 291–308, 2002.

[11] P. Fajfar, D. Marusić, I. Perus, Torsional effects in the pushover-based seismic analysis of buildings. Journal of Earthquake Engineering, **9**, 831–854, 2005.

[12] C. Bhatt, R. Bento, Assessing the seismic response of existing RC buildings using the extended N2 method. Bulletin of Earthquake Engineering, **9**, 1183–1201, 2011.

[13] A. K. Chopra, and R. K. Goel, A modal pushover analysis procedure to estimate seismic demands for unsymmetric-plan buildings, Earthquake Engineering and Structural Dynamics **33**, 903–927, 2004.

[14] M. Bosco, A. Ghersi, E. M. Marino, Corrective eccentricities for assessment by nonlinear static method of 3D structures subjected to bidirectional ground motion. Earthquake Engineering and Structural Dynamics, **41**, 1751–1773, 2012.

[15] K. Fujii, Nonlinear static procedure for multi-story asymmetric frame buildings considering bidirectional excitation. Journal of Earthquake Engineering, **15**, 245–273, 2011.

[16] K. Fujii, Prediction of the largest peak nonlinear seismic response of asymmetric buildings under bi-directional excitation using pushover analyses, Bulletin of Earthquake Engineering, **12**, 909-938, 2014.

[17] R. Kinoshita, K. Miyagawa, M. Haginoya, K. Fujisawa, K. Imai, Y. Ohtani, I Mitani, Study on seismic retrofit for existing R/C buildings by using CHS bracing, Proceedings of First fib Congress, 505-514, Osaka, Japan, October 13-19, 2002.

[18] T. Ishiii, T. Mukai, H. Kitamura, T. Shimizu, K. Fujisawa, and Y. Ishida, Seismic retrofit for existing R/C building using energy dissipative braces, Proceedings of 13th World Conference on Earthquake Engineering, paper no. 1209, Vancouver, Canada, August 1-6, 2004.

[19] S. Otani, New seismic design provision in Japan, Proceeding of the Second U.S.-Japan Workshop on Performance-Based Earthquake Engineering Methodology for Reinforced Concrete Structures. PEER report, 10, 3–14, 2000.

[20] AIJ, Design guidelines for earthquake resistant reinforced concrete buildings based on inelastic displacement concept. Architectural Institute of Japan, Tokyo, 1999. (Japanese)

[21] K. Muto, T. Hisada, T. Tsugawa, and S. Bessho, Earthquake resistant design of a 20 story reinforced concrete buildings. Proceedings of the 5th World Conference on Earthquake Engineering, 1960–1969, Rome, Italy, 1974.

[22] S. Otani, Hysteresis models of reinforced concrete for earthquake response analysis, Journal of Faculty of Engineering University of Tokyo, **36(2)**, 407–441, 1981.

[23] K. Fujii, T. Ikeda, Shaking table test of irregular buildings under horizontal excitation acting in an arbitrary direction, Proceedings of 15th World Conference on Earthquake Engineering, paper no. 0439, Lisbon, Portugal, September 24-28, 2012.

[24] K. Fujii, Torsional Index of asymmetric building based on mode shape, Proceedings of the 7th European Workshop on the Seismic Behaviour of Irregular and Complex Structures, paper no. 14, Faculty of Civil Engineering, Opole University of Technology, Poland, October 17-18, 2014.

[25] BCJ, The building standard law of Japan on CD-ROM. The Building Center of Japan, Tokyo, 2010.

[26] A. López, JJ. Hernández, R. Bonilla, A. Fernández, Response spectra for multicomponent structural analysis, Earthquake Spectra, **22**, 85–113, 2006.

[27] T. Isakovic, M. Fischinger, Applicability of pushover methods to the seismic analysis of an RC bridge, experimentally tested on three shake tables. Journal of Earthquake Engineering, **15**, 303–320, 2011.